Acta Oceanol. Sin., 2018, Vol. 37, No. 7, P. 85–104
DOI: 10.1007/s13131-018-1247-8
http://www.hyxb.org.cn
E-mail: hyxbe@263.net

An analytical approximation of focusing-wave-induced load on a semi-submerged cylinder

HU Zhe[1, 2], ZHANG Xiaoying[1, 2*], LI Yan[1, 2], LI Xiaowen[1, 2]

[1] Key Laboratory of Fujian Province for Ships and Ocean Engineering, Jimei University, Xiamen 361021, China

[2] School of Marine Engineering, Jimei University, Xiamen 361021, China

Received 14 June 2017; accepted 10 October 2017

Abstract

Owing to the complexity of the physical mechanisms of rouge waves, the theoretical study of the rogue-wave-structure interaction problems still makes little progress. However, for regular-shaped structures, it is possible to give a theoretical analysis, if a relatively simple model of the rogue waves is used. The wave load, induced by a focusing wave which is known as an intuitive basic model of the rouge waves, upon a semi-submerged cylinder is studied analytically. The focusing wave is approximate by the Gauss envelope wave, an ideal model which contains most features of the rogue wave. The diffraction velocity potential is derived through the separation of flow field, and the formulas of the horizontal force and bending moment are proposed. The derived formulas are simplified appropriately, and validated through comparison against numerical results. In addition, the influence of parameters, such as the focusing degree, the submerging depth and the wave focusing position, is thoroughly investigated.

Key words: focusing wave, Gauss envelope, semi-submerged cylinder, potential theory, analytical solution

Citation: Hu Zhe, Zhang Xiaoying, Li Yan, Li Xiaowen. 2018. An analytical approximation of focusing-wave-induced load on a semi-submerged cylinder. Acta Oceanologica Sinica, 37(7): 85–104, doi: 10.1007/s13131-018-1247-8

1 Introduction

Rogue waves are usually defined as waves whose height exceeds the significant wave height in two times. The rogue waves happen under various conditions, and live only for a short time, making them difficult to predict. The research around the rogue waves has been carried out from three aspects: the physical models of the rogue waves, the generation of the rogue waves under laboratory and numerical wave tanks, and the interaction between the rouge waves and structures. The first aspect focuses on the theoretical background of the rogue waves, and aims at finding the nature of the rogue waves. The last aspect is closely related to realistic engineering problems, and its final purpose is to find how structures can remain safety during the severe impact caused by the rogue waves. The second aspect acts as a connection between the first and last aspects, and its motivation is to generate the rogue waves correctly, in order to help better understand their inherent features and to apply them to the study of wave-structure issues.

The physical mechanisms of the rouge waves have attracted the interest of many researchers, due to their special characteristics such as the sudden occurrence, the short-living lifespan, the extremely high crest and largely asymmetric appearance. Most study lies within the area of nonlinearity wave mechanics. Some popular models of the rouge waves consist of the nonlinear Schrödinger (NLS) equation under finite and deep water (Hu et al., 2015), the Korteweg-de Vries (KdV) equation (Kit et al., 2000), and the more universe Euler equations and N-S equations. Within these models, the rogue waves are explained as driven by the modulational instability or Benjamin-Feir instability (Osborne et al., 2000; Zakharov et al., 2006), or as certain breather solutions (He et al., 2013; Qin et al., 2017). Kharif and Pelinovsky (2003) gave a comprehensive summery of the existing physical mechanisms of the rogue waves. Recently, the research into rogue-wave models has gone to higher-order nonlinearity (Weerasekara and Maruta, 2017; Yu and Yan, 2014), higher-order breathers (He et al., 2013) or higher-order Stokes components (Hu et al., 2015a).

Early generation methods of the rogue waves under laboratories and numerical tanks mainly rely on the linear superposition method, namely, the focusing model. The most widely used method is the superposition of a focusing wave train and a random wave field (Gao et al., 2016). Recent study has turned to nonlinear models such as the breather model. For instance, Chabchoub et al. (2011, 2012a) generated the breather-based rogue waves on the foundation of the cubic NLS equation under deep water in laboratory. Onorato et al. (2013) generated the breather-based rogue waves under a finite water depth in laboratory, and investigated the response of a scaled chemical tanker hit by the generated rogue waves. Chabchoub et al. (2012b) observed a hierarchy of up to fifth-order breather-type rogue waves in a water tank under the deep water. Slunyaev et al. (2013) studied the existence of stable strongly nonlinear groups of deep-water waves by means of laboratory and numerical simulations, and obtained very good agreement. Although nonlinear models have been applied to a rogue-wave generation in laboratories, the focusing model is still widely adopted. In laboratories and numerical wave tanks, the linear superposition of wave trains is prob-

Foundation item: The National Natural Science Foundation of China under contract No. 51609101; the Natural Science Foundation of Fujian Province of China under contract Nos 2017J01701 and 2017J05085.
*Corresponding author, E-mail: zhangxy@jmu.edu.cn

ably still the only way to generate a rogue wave with randomness features.

Compared with the study of physical models and generation methods, the research on wave-structure interaction seems to be still not adequate. Although there are studies which utilize nonlinear wave models (e.g., Hu et al., 2015b), due to the complexity of the nonlinear rogue wave models, the linear focusing model is still often used, since it reduces the complexity of the problem to a large extent, and simultaneously reflects most features of the rogue waves. Soares et al. (2006) calculated the response of a FPSO under the same rogue wave, using a nonlinear time-domain potential-theory solver. Sundar et al. (1999) studied the rogue-wave-induced loads on cylinders with various inclined angles. By now, most researches into rogue-wave-structure interaction problems rely on commercial numerical solvers or on the basis of experimental results. Deng et al. (2016) presented an experimental investigation on the rogue waves and the corresponding wave forces acting on a vertical cylinder. By contrast, theoretical study of these problems can be seldom found. Usually, it is complicated to model the rogue waves alone in an analytical manner (especially when nonlinear effect is taken into account), not to mention to formulate the wave-structure interaction problem. However, if regular-shaped structure is selected together with a linear model of the rogue waves, it is possible to give an analytical result. Though the linear model neglects nonlinearity effects, it still reflects many important naturals of the rogue waves, and the resulted solutions can reveal some features of the wave-structure interaction.

In this paper, we analytically approximate the wave-induced load when a semi-submerged cylinder is placed at the rogue wave field. To reduce the difficulty of solution, the rogue wave is modeled by the Gauss envelope, which is a fundamental wave in the focusing model (Kharif and Pelinovsky, 2003). The fluid flow around the upright cylinder is solved within the potential theory, and the expressions of the horizontal force and bending moment are derived. Furthermore, the convergence behavior of the progression solution is studied and the solution is divided into two categories, and is simplified appropriately. The proposed formulas are validated against numerical results, and the influence of various parameters on the wave load is analyzed.

The main content of the paper is organized as follows: in Section 2, we deduce the expressions of the wave load when the cylinder is subject to a linear monochromatic wave, which is the foundation of the focusing-wave condition; Section 3 gives an introduction to the Gauss envelope, and derived a horizontal force and bending moment induced by the Gauss-focusing wave; Section 4 verifies the proposed formulas by making comparison against the results obtained with a commercial potential-theory solver–WADAM; Section 5 discusses the analytical solution by analyzing the influence of various parameters; and the conclusions of this study are reported in Section 6.

2 Load induced by a monochromatic wave

In this section, the wave load induced by a linear monochromatic wave is studied, which is the foundation of the analysis of the focusing wave.

2.1 *Governing equations and solutions*

Figure 1 depicts a simple description of the problem, where R is the radius of the cylinder, h is the water depth, and d is the height of the submerging part of the cylinder. The origin of the coordinate system is located at the still water line (SWL), with z-axis coinciding with the symmetry axis of the cylinder. The incident wave propagates along the x+ direction. To simplify the problem, the entire computational domain is divided into two subdomains, i.e., Ω_1 and Ω_2. Ω_1 stands for the region $-h < z < 0$ and $r > R$, and Ω_2 $-h < z < -d$ and $r < R$. Here r denotes the distance from the cylinder symmetry axis.

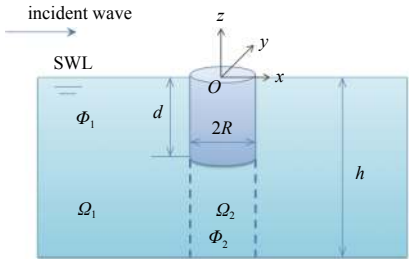

Fig. 1. Problem description of the incident wave meeting an upright submerged cylinder.

By ignoring the viscosity and surface tension of water, the problem can be solved using the potential theory. Let $\Phi_1 e^{-i(kx_0+\omega t)}$ and $\Phi_2 e^{-i(kx_0+\omega t)}$ be the velocity potentials of Ω_1 and Ω_2, where i is imaginary unit, k and ω are the wave number and angular frequency of the incident wave, respectively. x_0 stands for the focusing position of the rogue wave, which will be used later in Section 3. The governing equations are written as

$$\left.\begin{aligned} &\Delta\Phi_1 = 0 && \text{in} \quad -h < z < 0,\ r > R \\ &\frac{\partial\Phi_1}{\partial z} = 0 && \text{on} \quad z = -h \\ &-\omega^2\Phi_1 + g\frac{\partial\Phi_1}{\partial z} = 0 && \text{on}\ z = 0 \end{aligned}\right\}, \tag{1}$$

$$\left.\begin{aligned} &\Delta\Phi_2 = 0 && \text{in} \quad -h < z < -d,\ r < R \\ &\frac{\partial\Phi_2}{\partial z} = 0 && \text{on} \quad z = -h \\ &\frac{\partial\Phi_2}{\partial z} = 0 && \text{on} \quad z = -d \end{aligned}\right\}. \tag{2}$$

The two velocity potentials are connected by

$$\frac{\partial\Phi_1}{\partial r} = \begin{cases} 0 & \text{on}\ r = R,\ -d < z < 0, \\ \dfrac{\partial\Phi_2}{\partial r} & \text{on}\ r = R,\ -h < z < -d, \end{cases} \tag{3}$$

$$\Phi_1 = \Phi_2 \qquad \text{on}\ r = R,\ -h < z < -d. \tag{4}$$

The velocity potential Φ_1 can be written as the summation of the incident-wave potential $\Phi_{1,\,\mathrm{i}}$ and the diffraction potential $\Phi_{1,\,\mathrm{d}}$. The incident potential (namely, the linear-wave potential), formulated under the cylindrical coordinate, can be written as

$$\left.\begin{aligned} &\Phi_{1,\,\mathrm{i}} = \frac{\mathrm{i}g\cosh k(z+h)}{\omega\cosh kh}\sum_{n=0}^{\infty}\beta_n \mathrm{J}_n(kr)\cos n\theta \\ &\beta_n = \begin{cases} 1 & n = 0 \\ 2\mathrm{i}^n & n \geqslant 1 \end{cases} \end{aligned}\right\}, \tag{5}$$

where J_n is the first-kind Bessel function. Equation (5) is deduced by using the Bessel-function expansion on term e^{ikx}.

The diffraction potential can be also written in the expansion

form, as

$$\Phi_{1,\,\mathrm{d}}=\sum_{n=0}^{\infty}\left\{\begin{array}{l}\left[\alpha_{n,\,0}\mathrm{H}_n^{(1)}(kr)+\beta_{n0}H_n^{(2)}(kr)\right]\times\\ \cosh\left[k(z+h)\right]+\\ \sum\limits_{l=1}^{\infty}\left[\alpha_{n,\,l}\mathrm{K}_n(k_lr)+\beta_{n,\,l}\mathrm{I}_n(k_lr)\right]\times\\ \cos\left[k_l(z+h)\right]\end{array}\right\}\cos n\theta, \quad (6)$$

$$\omega^2=gk\tanh kh, \quad (7)$$

$$k_l \text{ is the } l-\text{th root of } \omega^2=-gk_l\tan k_lh, \quad (8)$$

where $\mathrm{H}_n^{(1)}$ and $\mathrm{H}_n^{(2)}$ are the first- and second-kind Hankel functions, and I_n and K_n are the first- and second-kind modified Bessel functions, respectively. Since $\mathrm{H}_n^{(2)}(kr)$ and $\mathrm{I}_n(k_lr)$ in Eq. (6) contradicts against the radiation condition when $r\to\infty$, $\beta_{n,0}$ and $\beta_{n,l}$ should be 0, i.e.,

$$\Phi_{1,\,\mathrm{d}}=\sum_{n=0}^{\infty}\left\{\alpha_{n,0}\frac{\mathrm{H}_n(kr)}{\mathrm{H}_n(kR)}\frac{\cosh\left[k(z+h)\right]}{\cosh kh}+\sum_{l=1}^{\infty}\alpha_{n,\,l}\frac{\mathrm{K}_n(k_lr)}{\mathrm{K}_n(k_lR)}\frac{\cos\left[k_l(z+h)\right]}{\cos k_lh}\right\}\cos n\theta, \quad (9)$$

where H_n is short for $\mathrm{H}_n^{(1)}$.

Similarly, the series expansion on the velocity potential Φ_2 is written as

$$\Phi_2=\sum_{n=0}^{\infty}\left\{\gamma_{n,\,0}\left(\frac{r}{R}\right)^n+\sum_{j=1}^{\infty}\gamma_{n,\,j}\frac{\mathrm{I}_n(m_jr)}{\mathrm{I}_n(m_jR)}\frac{\cos\left[m_j(z+h)\right]}{\cos(m_jh)}\right\}\cos n\theta, \quad (10)$$

$$m_j=\frac{j\pi}{h-d}, \quad (11)$$

noted that Φ_2 should be bounded at $r=0$. It can be easily verified that Eqs (9) and (10) satisfy Eqs (1) and (2), respectively. The unknown $\alpha_{n,\,l}$ and $\gamma_{n,\,j}$ can be determined by using Eqs (3) and (4), and the detailed derivation is listed in Appendix A.

After the unknown $\alpha_{n,\,l}$ and $\gamma_{n,\,j}$ are obtained, the sectional force is formulated as

$$F_R=-\int_0^{2\pi}pR\cos\theta\mathrm{d}\theta=-\mathrm{i}\omega\rho R\pi\mathrm{e}^{-\mathrm{i}(kx_0+\omega t)}\left\{\begin{array}{l}\left[\alpha_{10}+\dfrac{\mathrm{i}g\beta_1J_1(kR)}{\omega}\right]\times\\ \dfrac{\cosh\left[k(z+h)\right]}{\cosh kh}+\\ \sum\limits_{l=1}^{\infty}\alpha_{1,l}\dfrac{\cos\left[k_l(z+h)\right]}{\cos k_lh}\end{array}\right\}, \quad (12)$$

The horizontal force and the bending moment are

$$F=\int_{-d}^{0}F_R\mathrm{d}z=-\mathrm{i}\omega\rho R\pi\mathrm{e}^{-\mathrm{i}(kx_0+\omega t)}\times\left\{\begin{array}{l}\left[\alpha_{1,\,0}+\dfrac{\mathrm{i}g\beta_1J_1(kR)}{\omega}\right]\times\\ \dfrac{\sinh kh-\sinh\left[k(h-d)\right]}{k\cosh kh}+\\ \sum\limits_{l=1}^{L}\alpha_{1,\,l}\dfrac{\sin k_lh-\sin\left[k_l(h-d)\right]}{k_l\cos k_lh}\end{array}\right\}, \quad (13)$$

$$\begin{aligned}M&=\int_{-d}^{0}zF_R\mathrm{d}z-\int_0^R\mathrm{d}r\int_0^{2\pi}pr^2\cos\theta\mathrm{d}\theta\\&=-\mathrm{i}\omega\rho R\pi\mathrm{e}^{-\mathrm{i}(kx_0+\omega t)}\times\left\{\begin{array}{l}\left[\alpha_{1,0}+\dfrac{\mathrm{i}g\beta_1J_1(kR)}{\omega}\right]\times\\ \left\{\dfrac{\cosh\left[k(h-d)\right]+dk\sinh\left[k(h-d)\right]}{k^2\cosh kh}-\right\}-\\ \dfrac{1}{k^2}\\ \sum\limits_{l=1}^{L}\alpha_{1,\,l}\left\{\dfrac{\cos\left[k_l(h-d)\right]+dk\sin\left[k_l(h-d)\right]}{k_l^2\cos k_lh}-\dfrac{1}{k_l^2}\right\}+\\ \dfrac{R^2}{2}\gamma_{1,0}+\sum\limits_{j=1}^{J}\dfrac{(-1)^j}{\cos(m_jh)}\dfrac{RI_2(m_jR)}{m_jI_1(m_jR)}\gamma_{1,j}\end{array}\right\}.\end{aligned} \quad (14)$$

It should be noted that only a finite number of expansion terms are kept in Eqs (13) and (14). To verify the above equations, the results predicted by Eqs (13) and (14) are compared with those calculated using a commercial potential-theory solver–WADAM. The WADAM is a general analysis program for calculation of the wave-structure interaction for the fixed and floating structures of arbitrary shape, e.g., semi-submersible platforms, tension-leg platforms, gravity-base structures and ship hulls. It solves diffraction issues of zero-speed floating bodies using a 3–D boundary element method (BEM) with free surface Green functions. The analysis capabilities in the WADAM comprise calculation of global responses of loads and motions including first- and second-order components. The Morison's equation can be also specified if slender structures are considered. The 3–D potential theory in WADAM is based directly on the Wamit program developed by Massachusetts Institute of Technology, which has been thoroughly verified.

Four test cases are performed, which are listed in Table 1. In Table 1, Case b is identical to Case a, except that a dense grid setting is used. Therefore, the results of Case a and Case b are displayed together in Fig. 2. The results of Case c and Case d are shown in Figs 3 and 4, respectively. As shown in Fig. 2, the results obtained with two sets of grid accord with each other, indicating that the grid setting is appropriate, and that the coarse grid set is enough for this problem. In Figs 2–4, the theoretical results agree well with the numerical ones, under various water depths, cylin-

Table 1. Parameters adopted in WADAM solver

Case	h/m	d/m	R/m	Grid (circumferential by vertical)
a	5	3	3.14	36 by 18 (coarse)
b	5	3	3.14	180 by 60 (dense)
c	20	3	3.14	36 by 18 (coarse)
d	20	15	3.14	36 by 18 (coarse)

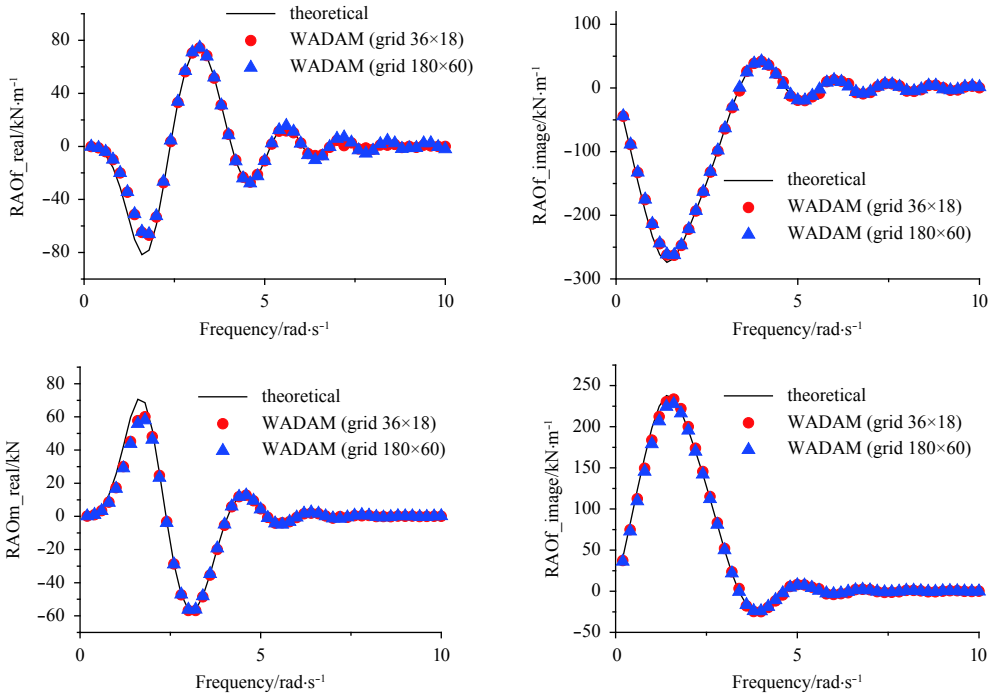

Fig. 2. RAOs of the horizontal force and the bending moment, computed with the parameters of Case a and Case b.

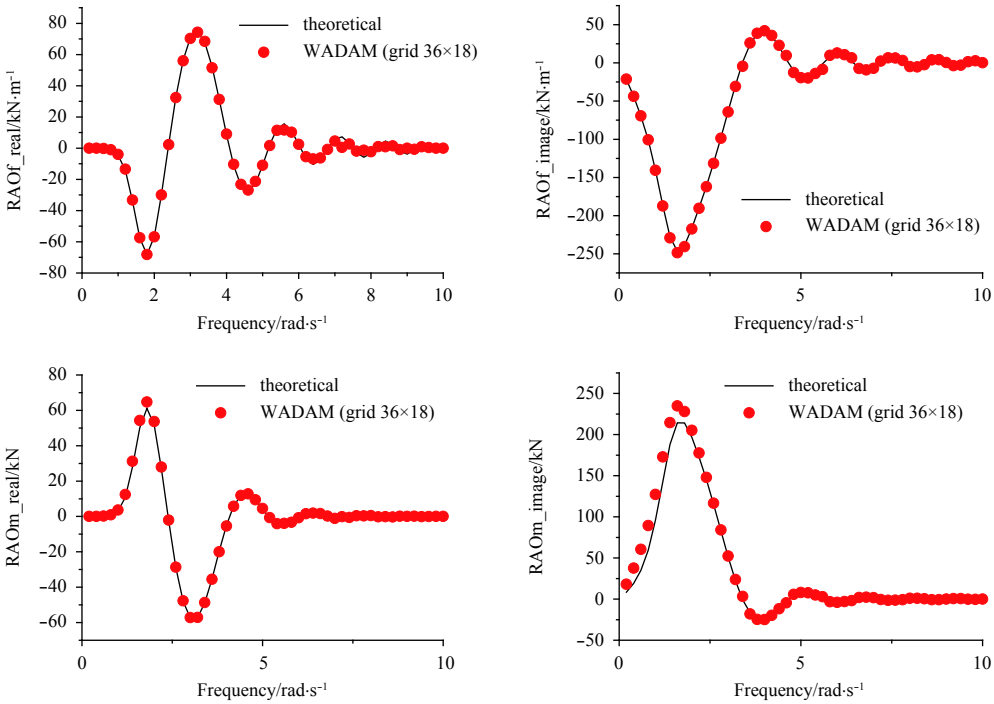

Fig. 3. RAOs of the horizontal force and the bending moment, computed with the parameters of Case c.

der lengths and wavelengths. This demonstrates the reliability of the theoretical formulas.

2.2 *Semi-submerged cylinder in finite-depth water*

Although Eqs (13) and (14) give exact formulation of the wave force and moment, it is not convenient to use them in realistic engineering applications. For instance, parameter $\alpha_{1,l}$ and $\gamma_{1,j}$ have to be predetermined by solving linear algebraic equations, and the results are written as the summation of series expansions rather than exact formulas. Therefore, simplification is made on Eqs (13) and (14) before further discussion.

First, the influence of the series expansion is studied. By computing the wave force and moment with various values of L and J, the influence of the summation terms can be estimated. Here, for most cases listed in Table 1, $L = J = 5$ is considered to be large enough to give precise results, noticing that the theoretical

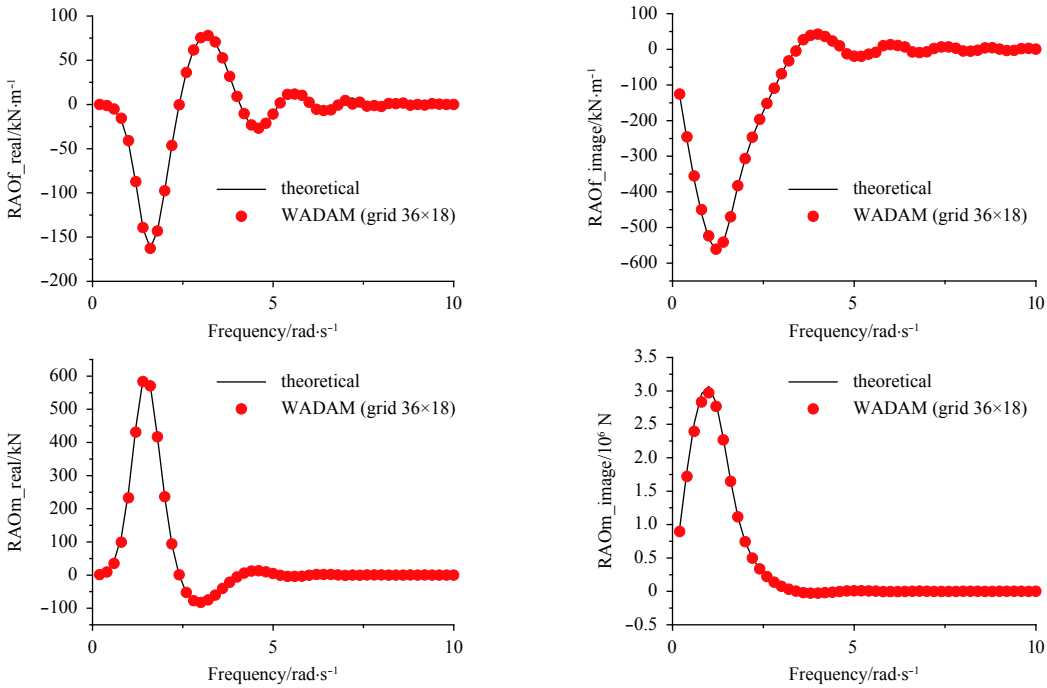

Fig. 4. RAOs of the horizontal force and the bending moment, computed with the parameters of Case d.

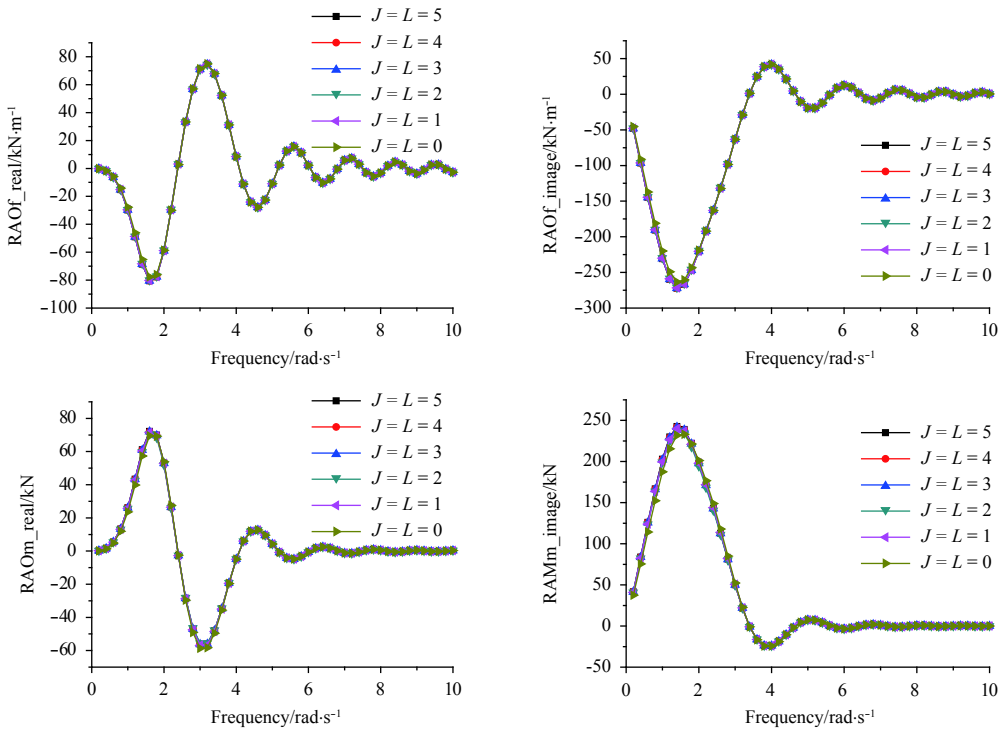

Fig. 5. RAOs of the horizontal force and bending moment with various truncated numbers of the series expansion, computed with the parameters of Case a.

curves in Figs 2–4 are obtained with $L = J = 5$. Figure 5 shows the wave force and moment computed with L and J changing from 0 to 5, using the parameters of Case a. Here, that L or J equals 0 means the summation of the series expansion vanishes. In Fig. 5, computation with various L and J almost gives the identical results, even when $L = J = 0$. This reveals that the summation terms of Eqs (13) and (14) are far smaller than the terms with respect to $\alpha_{1,0}$ and $\gamma_{1,0}$, for Case a.

Similar to Fig. 5, Figs 6 and 7 give the RAOs calculated with various L and J, using parameters of Case c and Case d, respectively. As shown in Fig. 7, $L = J = 0$ gives acceptable prediction when $h = 20$ m and $d = 15$ m. However, it causes non-ignorable deviation when $h = 20$ m and $d = 3$ m, which can be seen in Fig. 6. This is due to the fact that the terms related to $\gamma_{n,j}$ can no

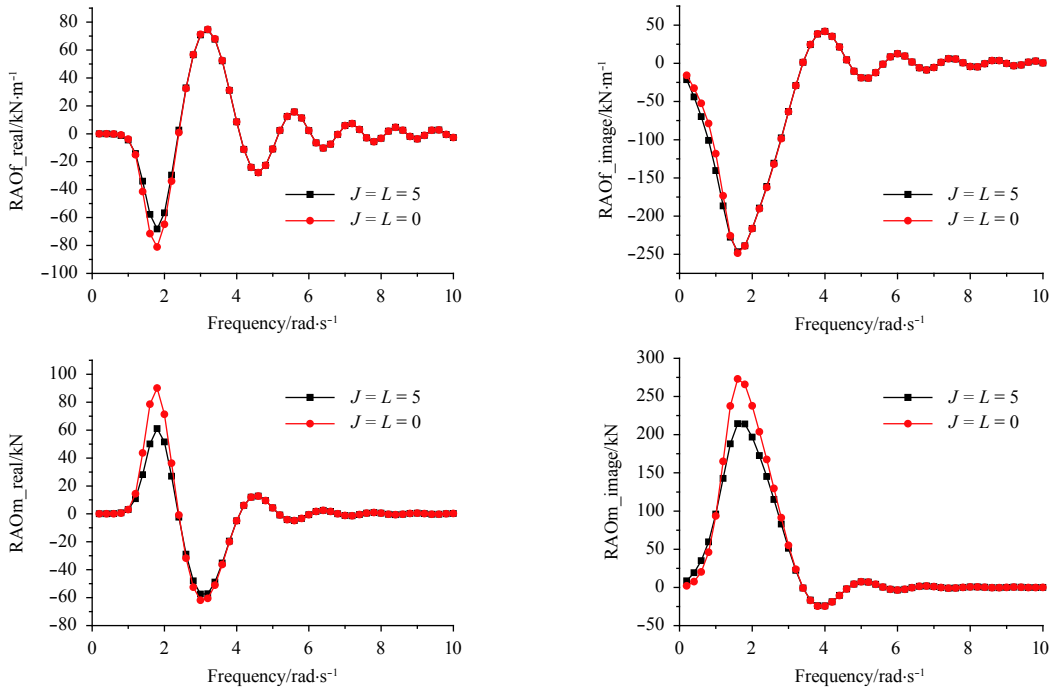

Fig. 6. RAOs of the horizontal force and bending moment with various truncated numbers of the series expansion, computed with the parameters of Case c.

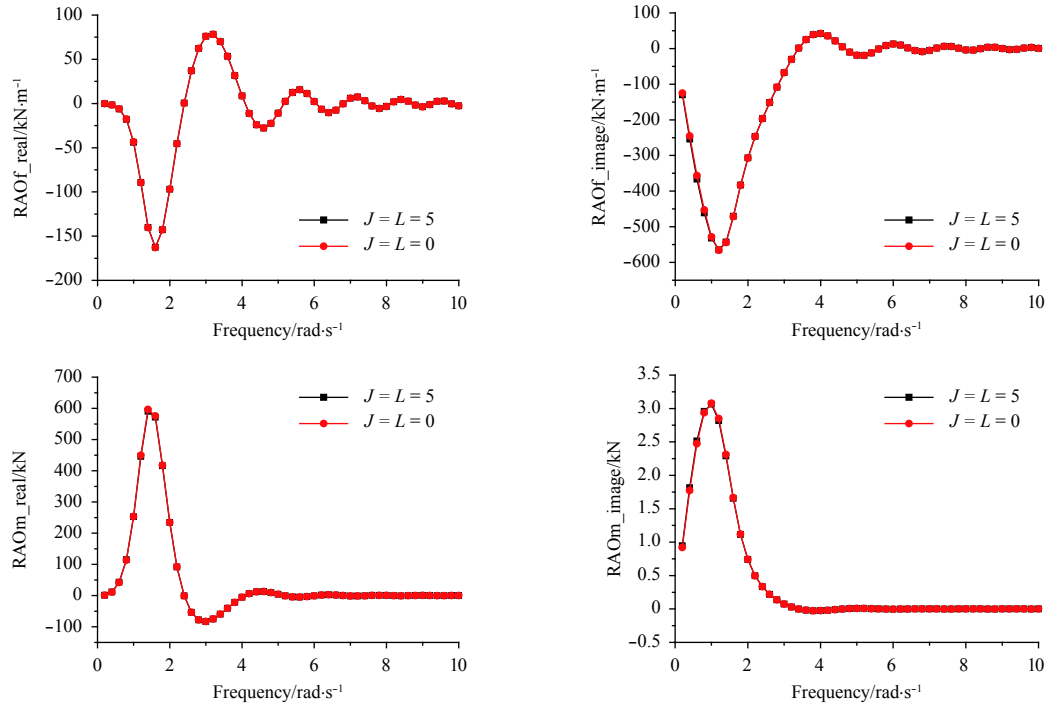

Fig. 7. RAOs of the horizontal force and bending moment with various truncated numbers of the series expansion, computed with the parameters of Case d.

longer be omitted. This fact causes the inherent difference between cylinders in the finite-depth water and in the deep water. Here, the term "finite-depth" means the water depth has the same order with the submerging length of the cylinder, and has a little difference between its common meaning in wave mechanics. To be specific, even if the water depth is fairly large, the term "finite-depth" still applies provided the submerging height of the cylinder is large enough such that $d/h \sim O(1)$. The term "deep" has its common meaning, i.e., $h \to \infty$, making both submerging height and wavelength far smaller by comparison. This subsection mainly deals with formulas in the finite-depth water, and the deep water condition will be discussed in Subsection 2.3.

As mentioned above, the summation terms of Eqs (13) and (14) can be omitted under the finite-depth water, and therefore the key is the determination of parameters $\alpha_{1,0}$ and $\gamma_{1,0}$. Let $\alpha^*_{1,0}=\alpha_{1,0}+\dfrac{\mathrm{i}g\beta_1\mathrm{J}_1(kR)}{\omega}$, and parameters $\gamma_{1,0}$ and $\alpha^*_{1,0}$ are governed by equations as follows (Eqs (A3) and (A5)):

$$\alpha^*_{1,0}=-\frac{4\mathrm{i}g}{\pi\omega kR\mathrm{H}'_1(kR)}+\frac{\sinh k(h-d)\times\mathrm{H}_1(kR)}{k^2R\cosh kh\times\mathrm{H}'_1(kR)\,\|Z_0\|^2}\gamma_{1,0}, \tag{15}$$

$$\gamma_{1,0}=\frac{\sinh k(h-d)}{kh\cosh kh}\alpha^*_{1,0}. \tag{16}$$

Equations (15) and (16) are derived using the identity $\mathrm{J}_n(kR)-\dfrac{\mathrm{J}'_n(kR)}{\mathrm{H}'_n(kR)}\mathrm{H}_n(kR)=\dfrac{2\mathrm{i}}{\pi kR\mathrm{H}'_n(kR)}$. Substituting Eq. (16) into Eq. (15), parameter $\alpha^*_{1,0}$ is written as

$$\alpha^*_{1,0}=\frac{1}{1-f(kh,\lambda_1)\cdot g(kh,\lambda_2)}\left[-\frac{4\mathrm{i}g}{\pi\omega kR\mathrm{H}'_1(kR)}\right], \tag{17}$$

$$f(kh,\lambda_1)=\frac{4\sinh^2(kh\lambda_1)}{2(kh)^2+kh\sinh(2kh)}, \tag{18}$$

$$g(kh\lambda_2)=\frac{\mathrm{H}_1(kh\lambda_2)}{kh\lambda_2\mathrm{H}'_1(kh\lambda_2)}, \tag{19}$$

where $\lambda_1=1-d/h\mathrm{i}$ and $\lambda_2=R/h\mathrm{i}$ and the term $-\dfrac{4\mathrm{i}g}{\pi\omega kR\mathrm{H}'_1(kR)}$, which can be found in may textbooks, corresponds to the basic solution when $d=h$, namely, when the cylinder extends from the still water surface to the bottom. Hence, Eq. (17) can be treated as the basic solution multiplied by a correction, and the correction is related to the relative extension (λ_1) and relative radius (λ_2) of the cylinder. The horizontal force and the bending moment are finally written as

$$F=-\mathrm{i}\omega\rho R\pi\mathrm{e}^{-\mathrm{i}(kx_0+\omega t)}\alpha^*_{1,0}\times\frac{\sinh kh-\sinh[k(h-d)]}{k\cosh kh}, \tag{20}$$

$$M=-\mathrm{i}\omega\rho R\pi\mathrm{e}^{-\mathrm{i}(kx_0+\omega t)}\left\{\alpha^*_{1,0}\times\left\{\frac{\cosh[k(h-d)]+dk\sinh[k(h-d)]}{k^2\cosh kh}-\frac{1}{k^2}\right\}+\frac{R^2}{2}\gamma_{1,0}\right\}. \tag{21}$$

2.3 *Semi-submerged cylinder in deep water*

It is found during application that the finite-depth approximation shows a distinctive deviation against the exact solution when $d/h<0.25$. Under such condition, the deep-water solution applies. The deep-water condition is much more complex than the case under the finite water depth. Not only the summation terms of Eqs (13) and (14) affect the calculation results, but also the series expansions own a bad convergence rate, making it difficult to compute the wave force and moment precisely. Here we give a brief analysis of the phenomenon qualitatively. To simplify the discussion, let $h\to\infty$ and $d\to0$ simultaneously, and the unknown $\alpha_{n,l}$ and $\gamma_{n,j}$ of Eqs (9) and (10) are decided by the equations as (see Appendix B for details)

$$\alpha_{1,0}\to-\frac{\mathrm{i}g\beta_1\mathrm{J}'_1(kR)\mathrm{H}_1(kR)}{\omega\mathrm{H}'_1(kR)}+\sum_{j=0}^{\infty}\frac{2\mathrm{H}_1(kR)}{kR\mathrm{H}'_1(kR)}\gamma_{1,j}, \tag{22}$$

$$\alpha_{1,l}\to\frac{2}{k\cdot h}\sum_{j=0}^{\infty}\frac{(k_lh)^2}{(k_lh)^2-(m_jh)^2}\gamma_{1,j}, \tag{23}$$

$$\gamma_{1,0}\to\frac{\mathrm{i}g\beta_1\mathrm{J}_1(kR)}{\omega kh}+\frac{1}{kh}\alpha_{1,0}-kh\sum_{l=1}^{\infty}\frac{1}{(k_lh)^2}\alpha_{1,l}, \tag{24}$$

$$\gamma_{1,j}\to2\frac{\mathrm{i}g\beta_1\mathrm{J}_1(kR)}{\omega kh}+2\frac{1}{kh}\alpha_{1,0}-2kh\sum_{l=1}^{\infty}\frac{1}{(k_lh)^2-(m_jh)^2}\alpha_{1,l}. \tag{25}$$

Let $\alpha_{n,0}\approx O(h^a)$, $\alpha_{n,l}\approx O(h^b)$, $\gamma_{n,0}\approx O(h^c)$ and $\gamma_{n,j}\approx O(h^d)$ and thereby a, b, c and d have the relationship as follows:

$$\left.\begin{aligned}a&=\max(0,c,d)\\b&=\max(c-1,d-1)\\c&=\max(-1,a-1,b+1)\\d&=\max(-1,a-1,b+1)\end{aligned}\right\}. \tag{26}$$

From Eq. (26), one can easily obtain that $c=d=b+1$ and $a=b+1$ or $a=b+2$. If $a=b+1$, then $c\geqslant0$ and $d\geqslant0$. This indicates that the "constant" term - $\dfrac{\mathrm{i}g\beta_n\mathrm{J}_n(kR)}{\omega kh}$ in Eqs (24) and (25) is of higher order and should be neglected. However, this will make the entire linear equation system has infinite number of solutions or trivial solution. To make the solution meaningful (i.e., the "constant" term should be reserved), c and d must equal -1. Therefore, $a=0$, $b=-2$ and $c=d=-1$. Although Eqs (22)–(25) are derived under the condition that $h\to\infty$ and $d\to0$, it should be noted that the value of d does not affect the relationship of orders listed in Eq. (26), and it only makes the terms of Eqs (22)–(25) more complex and tedious to formulate. Here, $d\to0$ is only used to make the equations simpler, and it is not an indispensable requirement of this subsection.

From the above discussion, by omitting higher-order components, the horizontal force and the bending moment can be formulated as

$$F=-\mathrm{i}\omega\rho R\pi\mathrm{e}^{-\mathrm{i}(kx_0+\omega t)}\alpha'_{1,0}\frac{1-\mathrm{e}^{-kd}}{k}, \tag{27}$$

$$M=-\mathrm{i}\omega\rho R\pi\mathrm{e}^{-\mathrm{i}(kx_0+\omega t)}\left\{\alpha'_{1,0}\frac{\mathrm{e}^{-kd}+dk\mathrm{e}^{-kd}-1}{k^2}+R^2\left[\frac{\gamma_{1,0}}{2}+\sum_{j=1}^{J}C_j\gamma_{1,j}\right]\right\}, \tag{28}$$

where

$$\alpha'_{1,0}=-\frac{4\mathrm{i}g}{\pi\omega kR\mathrm{H}'_1(kR)}, \tag{29}$$

$$C_j=\frac{\mathrm{I}_2(m_jR)}{m_jR\mathrm{I}_1(m_jR)}. \tag{30}$$

Figure 8 shows the outline of function $C(x)=\dfrac{\mathrm{I}_2(x)}{x\mathrm{I}_1(x)}$. Usually, when h is not very large, namely m_jR is not a tiny number,

C_j tends to 0 rapidly and the summation converges fast. However, when $h \to \infty$, C_j always tends to a constant (0.25 from Fig. 8) unless J is large enough. This means a large number of terms are required to reach convergence.

Figure 9 displays the RAOs of the bending moment, computed with various J and L. The parameters used in Fig. 9 are identical to those listed in test Case c except that h is 3 000 m here, i.e., the deep-water condition is adopted. As is shown in Fig. 9, the accurate solution can be obtained only when L and J are large enough. Hence, Eq. (28) has little value for realistic applications, if no simplification is made. From Eqs (24) and (25), one can find that $\gamma_{1,j} \propto a'_{1,0}$, and therefore we assume that Eq. (28) can be rewritten as

$$M = -\mathrm{i}\omega\rho R\pi \mathrm{e}^{-\mathrm{i}(kx_0+\omega t)} a'_{1,0} \times \left\{ f_1 \frac{\mathrm{e}^{-kd} + dk\mathrm{e}^{-kd} - 1}{k^2} + f_2 R^2 \mathrm{e}^{-kd} \right\}. \tag{31}$$

By conducting a series of simulations with various R/d, we give the approximation of f_1 and f_2 as follows:

$$\left.\begin{aligned} f_1 &= 2 - 1.143\mathrm{e}^{-0.369\,8\frac{R}{d}} + 0.002\,612\left(\frac{R}{d}\right)^{3.156} \\ f_2 &= 0.018\,84\left(\frac{R}{d}\right)^{0.645\,2} + 0.346\,3\left(\frac{d}{R}\right)^{0.773\,3} \end{aligned}\right\}. \tag{32}$$

In order to validate Eqs (31) and (32), Fig. 10 compares the moment-RAOs computed using Eq. (21), Eq. (31) and WADAM, with a series of R/d-values listed in Table 2.

In Fig. 10, Eq. (31) gives the results that well agree with the numerical ones of the WADAM, yet the finite-water formula – Eq. (21) fails when R/d is large. It is worth noting that Eq. (21) can still give reliable prediction of the bending moment under the condition that R/d is small enough. This is due to the fact that the second term of Eq. (31) (i.e., the contribution from the tank bottom) becomes unimportant either when R becomes small or when the submerging length d becomes large. Another phenomenon which should be mentioned is that two peaks occur in Fig. 10-6. Figure 11 enlarges the plots of Fig. 10-6, where the double peaks can be observed more clearly. The double peaks are induced by the two terms, which correspond to the contribution from the upright wall and the bottom of the cylinder respectively, reaching their maximum crests at distinct frequencies. Moreover, when the contributions from the two terms have the same magnitude but opposite directions, a zero bending moment is reached! Since the finite-depth approximation wrongly estimates the influence of the bottom under the deep-water condition, Eq. (21) cannot reflect the double-peak phenomenon.

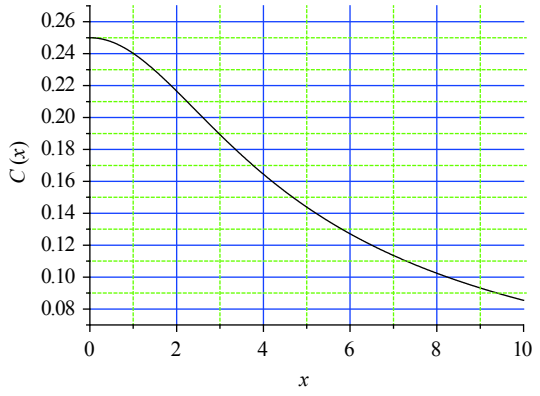

Fig. 8. Outline of function $C(x) = \mathrm{I}_2(x)/x\mathrm{I}_1(x)$.

3 Focusing-wave-induced load

Section 2 discusses the horizontal force and bending moment induced by monochromatic linear waves, and this section deals with the condition of focusing waves, which can be treated as the superposition of a series of fundamental wave components. From the point of view of the focusing model, the wave components of various amplitudes, frequencies and phases focus and yield a giant crest at a certain location and moment, which is a widely used model of the rouge waves. Among various kinds of focusing models, the Gauss-envelope-based model can explicitly give the expression of the surface elevation as well as the velocity potential, in relatively simple forms. Besides, it can explain most features of the rogue waves, for instance the large amplitude, energy focusing, short-living and occasional occurrence. As a result, the Gauss-envelope-based rogue wave has been thoroughly studied (see Kharif and Pelinovsky, 2003; Hu et al., 2014).

3.1 *Gauss envelope*

Hu et al. (2014) discussed the evolution of Gauss-envelope-based rogue waves in detail, from the point of view of the inversion problem of initial disturbances. Here, we directly list the corresponding equations of the Gauss envelope, without going into the detail of derivation. The free surface elevation and velocity potential of the Gauss envelope are written as

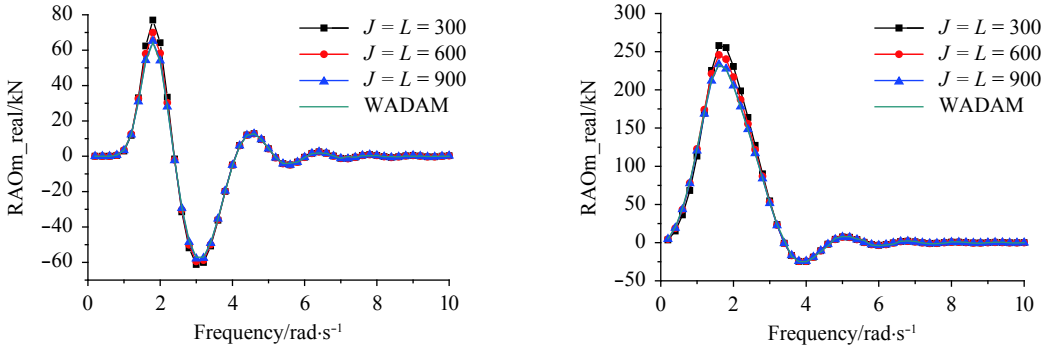

Fig. 9. RAOs of the bending moment computed with various truncated number of the series expansion, with the parameters of Case c except that $h = 3\,000$ m.

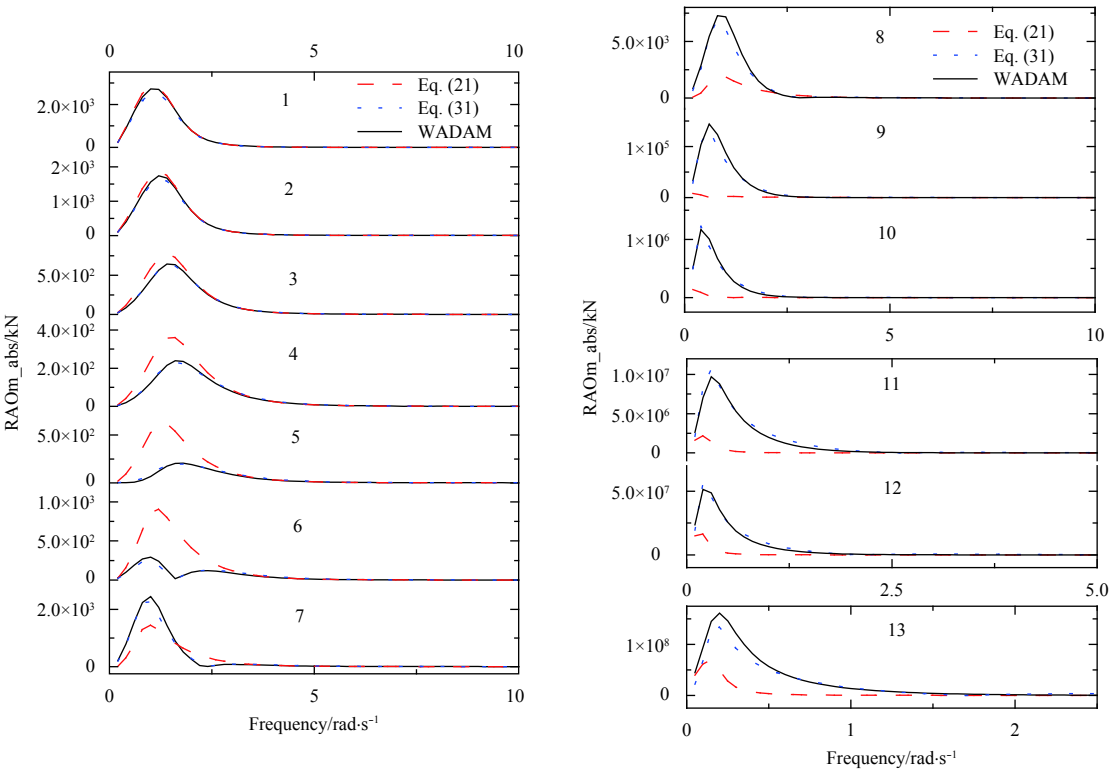

Fig. 10. RAOs of the bending moment predicted by Eq. (21), Eq. (31) and WADAM, computed with various R/d as listed in Table 2.

Table 2. Parameters used in Fig. 10 for the validation of Eqs (31) and (32)

Case	h/m	d/m	R/m	R/d
1	3 000	15	3.14	0.209
2	3 000	10	3.14	0.314
3	3 000	5	3.14	0.628
4	3 000	3	3.14	1.047
5	3 000	3	4.71	1.570
6	3 000	3	6.28	2.094
7	3 000	3	9.42	3.141
8	3 000	3	12.56	4.188
9	3 000	3	31.41	10.471
10	3 000	3	62.83	20.943
11	3 000	3	125.66	41.887
12	3 000	3	219.91	73.303
13	3 000	3	314.15	104.719

$$\zeta_{\mathrm{G}} = Re\left\{\frac{A_0\sigma \mathrm{e}^{\mathrm{i}[k_0(x-x_0)-\omega_0 t]}}{[\sigma^2+\mathrm{i}\omega''_0 t/2]^{1/2}}\exp\left[\frac{-[x-x_0-\omega'_0 t]^2}{4[\sigma^2+\mathrm{i}\omega''_0 t/2]}\right]\right\}, \quad (33)$$

$$\Phi_{\mathrm{G}} = Re\left\{-\mathrm{i}A_0\sigma\frac{g\cosh k_0(z+h)}{\omega_0\cosh k_0 h}\times \frac{\mathrm{e}^{\mathrm{i}[k_0(x-x_0)-\omega_0 t]}}{[\sigma^2+\mathrm{i}\omega''_0 t/2]^{1/2}}\exp\left[\frac{-[x-x_0-\omega'_0 t]^2}{4[\sigma^2+\mathrm{i}\omega''_0 t/2]}\right]\right\}, \quad (34)$$

where ω_0 and k_0 are the dominant angular frequency and wave number of the envelope. The rogue wave formulated in Eqs (33) and (34) reaches its maximum crest at $t=0$. This can be achieved by selecting the origin of the time axis such that the maximum wave crest occurs at $t=0$. Parameter σ controls the

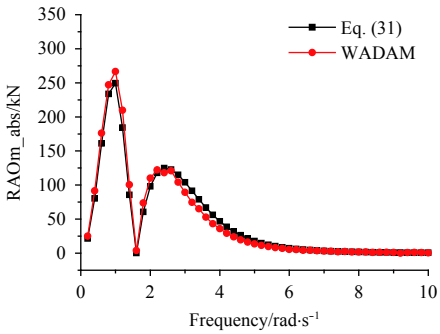

Fig. 11. Enlarged plots of Fig. 10-6.

bandwidth of the amplitude spectrum, which is formulated as

$$\hat{\zeta}_{\mathrm{G}} = \frac{A_0\sigma}{\sqrt{\pi}}\mathrm{e}^{-(k-k_0)^2\sigma^2}. \quad (35)$$

3.2 *Wave load*

Noticing that Section 2 gives the wave-induced load with respect to unit wave component $\mathrm{e}^{\mathrm{i}[k(x-x_0)-\omega t]}$, it will make the derivation intuitive and concise if the Gauss envelope is transformed into the superposition of unit waves. Using Eq. (35), the Gauss envelope can be rewritten as

$$\zeta_{\mathrm{G}} = \mathrm{Re}\left\{\int\frac{A_0\sigma}{\sqrt{\pi}}\mathrm{e}^{-(k-k_0)^2\sigma^2}\mathrm{e}^{\mathrm{i}[k(x-x_0)-\omega t]}\mathrm{d}k\right\}. \quad (36)$$

Hence, the Gauss-envelope-induced load under the finite-water depth can be written in integral form as

$$F=-\sqrt{\pi}\rho RA_0\sigma\times Re\left\{\mathrm{i}\int\omega\mathrm{e}^{-(k-k_0)^2\sigma^2}\mathrm{e}^{-\mathrm{i}(kx_0+\omega t)}\alpha^*_{1,0}Z_1(k)\,\mathrm{d}k\right\},\tag{37}$$

$$M=-\sqrt{\pi}\rho RA_0\sigma\,\mathrm{Re}\left\{\mathrm{i}\int\omega\mathrm{e}^{-(k-k_0)^2\sigma^2}\mathrm{e}^{-\mathrm{i}(kx_0+\omega t)}\times\left[\alpha^*_{1,0}Z_2(k)+\frac{R^2}{2}\gamma_{1,0}\right]\mathrm{d}k\right\},\tag{38}$$

where

$$Z_1(k)=\frac{\sinh kh-\sinh[k(h-d)]}{k\cosh kh},\tag{39}$$

$$Z_2(k)=\frac{\cosh[k(h-d)]+dk\sinh[k(h-d)]}{k^2\cosh kh}-\frac{1}{k^2}.\tag{40}$$

And the Gauss-envelope-induced load under the deep water depth can be written as

$$F=-\sqrt{\pi}\rho RA_0\sigma\times Re\left\{\mathrm{i}\int\omega\mathrm{e}^{-(k-k_0)^2\sigma^2}\mathrm{e}^{-\mathrm{i}(kx_0+\omega t)}\alpha'_{1,0}Z_3(k)\,\mathrm{d}k\right\},\tag{41}$$

$$M=-\sqrt{\pi}\rho RA_0\sigma\times Re\left\{\mathrm{i}\int\omega\mathrm{e}^{-(k-k_0)^2\sigma^2}\mathrm{e}^{-\mathrm{i}(kx_0+\omega t)}\alpha'_{1,0}Z_4(k)\,\mathrm{d}k\right\},\tag{42}$$

where

$$Z_3(k)=\frac{1-\mathrm{e}^{-kd}}{k},\tag{43}$$

$$Z_4(k)=f_1\frac{\mathrm{e}^{-kd}+dk\mathrm{e}^{-kd}-1}{k^2}+f_2R^2\mathrm{e}^{-kd}.\tag{44}$$

Since the amplitude spectrum of Gauss envelope owns a narrow bandwidth, the contribution from wave components whose wave numbers differ from k_0 is little. Therefore, ω is expanded into Taylor series around k_0, as $\omega=\omega_0+\omega'_0(k-k_0)+\frac{1}{2}\omega''_0(k-k_0)^2+\ldots$. Using this expansion, the integrals of Eqs (37)–(38) and (41)–(42) can be approximated as

$$F_{\mathrm{fi}}=d_0W_1X,\tag{45}$$

$$M_{\mathrm{fi}}=d_0W_2X,\tag{46}$$

$$F_{\mathrm{de}}=d_0W_3X,\tag{47}$$

$$M_{\mathrm{de}}=d_0W_4X,\tag{48}$$

where

$$d_0=-2\sqrt{2\pi A_0\sigma\rho gR},\tag{49}$$

$$W_1=W_0\frac{\sinh k_0h-\sinh[k_0(h-d)]}{k_0\cosh k_0h},\tag{50}$$

$$W_2=W_0\left\{\frac{\cosh[k_0(h-d)]+dk_0\sinh[k_0(h-d)]}{k_0^2\cosh k_0h}-\frac{1}{k_0^2}+\frac{R^2}{2}\frac{\sinh[k_0(h-d)]}{k_0h\cosh k_0h}\right\},\tag{51}$$

$$W_3=\frac{1-\mathrm{e}^{-k_0d}}{k_0},\tag{52}$$

$$W_4=f_1\frac{\mathrm{e}^{-k_0d}+dk_0\mathrm{e}^{-k_0d}-1}{k_0^2}+f_2R^2\mathrm{e}^{-k_0d},\tag{53}$$

$$W_0=\frac{1}{1-\dfrac{4\sinh^2[k_0(h-d)]}{2(k_0h)^2+k_0h\sinh(2k_0h)}\dfrac{\mathrm{H}_1(k_0R)}{k_0R\mathrm{H}'_1(k_0R)}},\tag{54}$$

$$X=\frac{1}{\sqrt{1/k_0R}+\mathrm{i}\sqrt{k_0R}}\frac{1}{(\sigma^2+\mathrm{i}\omega''_0t/2)^{1/2}}\times\exp\left[-\frac{(x_0+\omega'_0t+R)^2}{4(\sigma^2+\mathrm{i}\omega''_0t/2)}\right]\mathrm{e}^{-\mathrm{i}\left(k_0x_0+\omega_0t+k_0R-\frac{3}{4}\pi\right)},\tag{55}$$

note that the expressions of f_1 and f_2 are given by Eq. (32).

4 Validation

We give numerical validation on a large-scale cylinder under both finite-depth and deep-water conditions. 11 tests (Cases A to F correspond to the deep-water condition and the G-K finite-depth condition) are conducted and the corresponding parameters are listed in Table 3. As A_0 influences the simulated results in a linear manner, we set $A_0=0.15$ m in all the six tests. The water density is 1 025 kg/m^3. The Gauss-envelope focusing wave, lying within a frequency range of 0.2–10.0 rad/s, is divided into 50 unit waves with various amplitudes (this can be accomplished by discretizing Eq. (36)). The numerical results are obtained by superposing harmonic load components of various frequencies, whose amplitudes are predicted by the frequency solver WADAM. The time interval is 0.01 s, which equals 1/280–1/140 wave periods of the carriers listed in Table 3, which is enough to reveal the entire propagation process of the focusing waves. The theoretical results are calculated using Eqs (47) and (48) for the deep water.

To ensure the frequency division is reasonable and the generated waves are correct, Fig. 12 combines the 50 unit waves, and compares the resulted surface elevations with the ones predicted by Eq. (33). In Fig. 12, the superposition method gives almost the exactly same prediction as the theoretical calculation. It should be noted that the even division of frequency will result in a periodical surface-history pattern, which can be apparently observed in tests C, G and H. This phenomenon, however, does not affect the surface elevation in the vicinity of its maximum crest. Figure 12 indicates the frequency division is appropriate.

Figure 13 shows the time histories of the horizontal wave force and bending moment. If one neglects the periodical phenomenon induced by even division of frequency range in numer-

Table 3. Parameters used in the tests for numerical validation

Test	h/m	d/m	R/m	Wavelength/m	σ	x_0
A	3 000	3	6.28	6.28	6	0
B	3 000	3	12.54	12.54	6	0
C	3 000	15	3.14	3.14	6	0
D	3 000	3	6.28	6.28	4	0
E	3 000	3	6.28	6.28	4	10
F	3 000	15	3.14	6.28	6	10
G	20	15	3.14	3.14	6	0
H	5	3	3.14	3.14	6	0
I	20	15	6.28	6.28	6	0
J	20	15	3.14	3.14	4	0
K	20	15	3.14	3.14	4	10

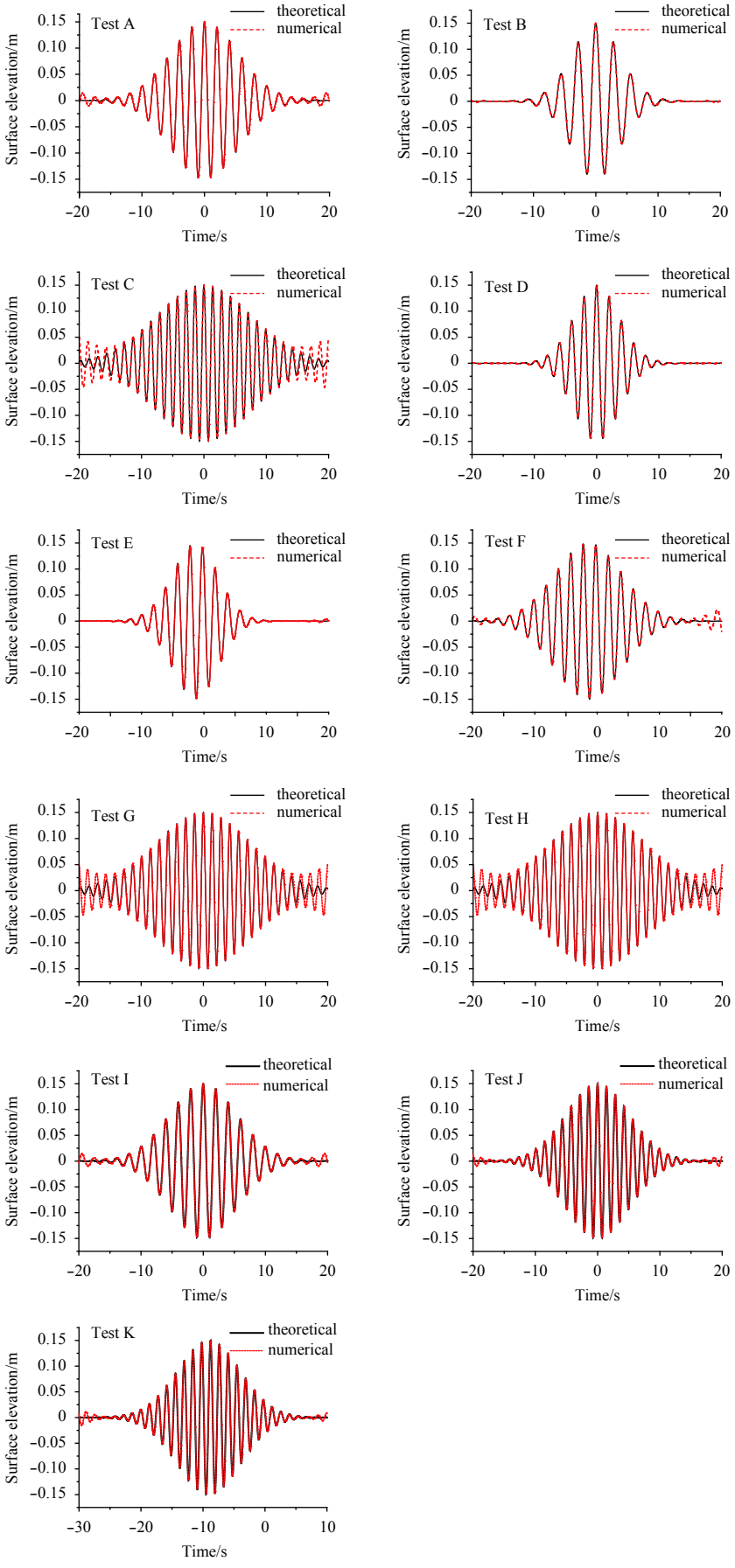

Fig. 12. Comparison of the numerical surface histories with the theoretical ones predicted by Eq. (33).

ical results, it can be observed that the theoretical results agree well with the numerical ones for most cases, which verifies the formulas proposed in this paper. It should be mentioned that $x_0 = 0$ in Tests A to D indicates that the maximum wave crest occurs at $x = 0$ and $t = 0$. However, the peak values of the wave load happen before $t = 0$. Further investigation points out that a large load can be induced when the maximum wave crest occurs somewhere in front of the cylinder, and this fact will be further discussed in Section 5.

For the purpose of investigating the deviation between the numerical and theoretical results, an envelope error curve is displayed in each subplot of Fig. 13. Among all subplots of Fig. 13, Test B seems to present relatively large errors, due to the fact that the wave number of the carrier wave of Test B is small in comparison with other test cases. In Eq. (35), one can observe that the amplitude spectrum will contain components with small wave numbers if k_0 (i.e., the wave number of the carrier) is small. Furthermore, if k_0 is small enough, wave components with zero and negative wave numbers can be involved. However, as is shown in Eqs (41)–(44), $k = 0$ is a singular point when determining the wave force and wave moment under deep water condition. In this paper, we process the integrals of Eqs (41) and (42) with a first-order approximation. Apparently, this approach can induce a non-negligible deviation in the vicinity of the singular point. It is worth noting that no singular point exists in the integral of surface elevation, which is formulated in Eq. (36). As a result, the theoretical surface elevation shows excellent agreement with the numerical one, which is displayed in Test B of Fig. 12.

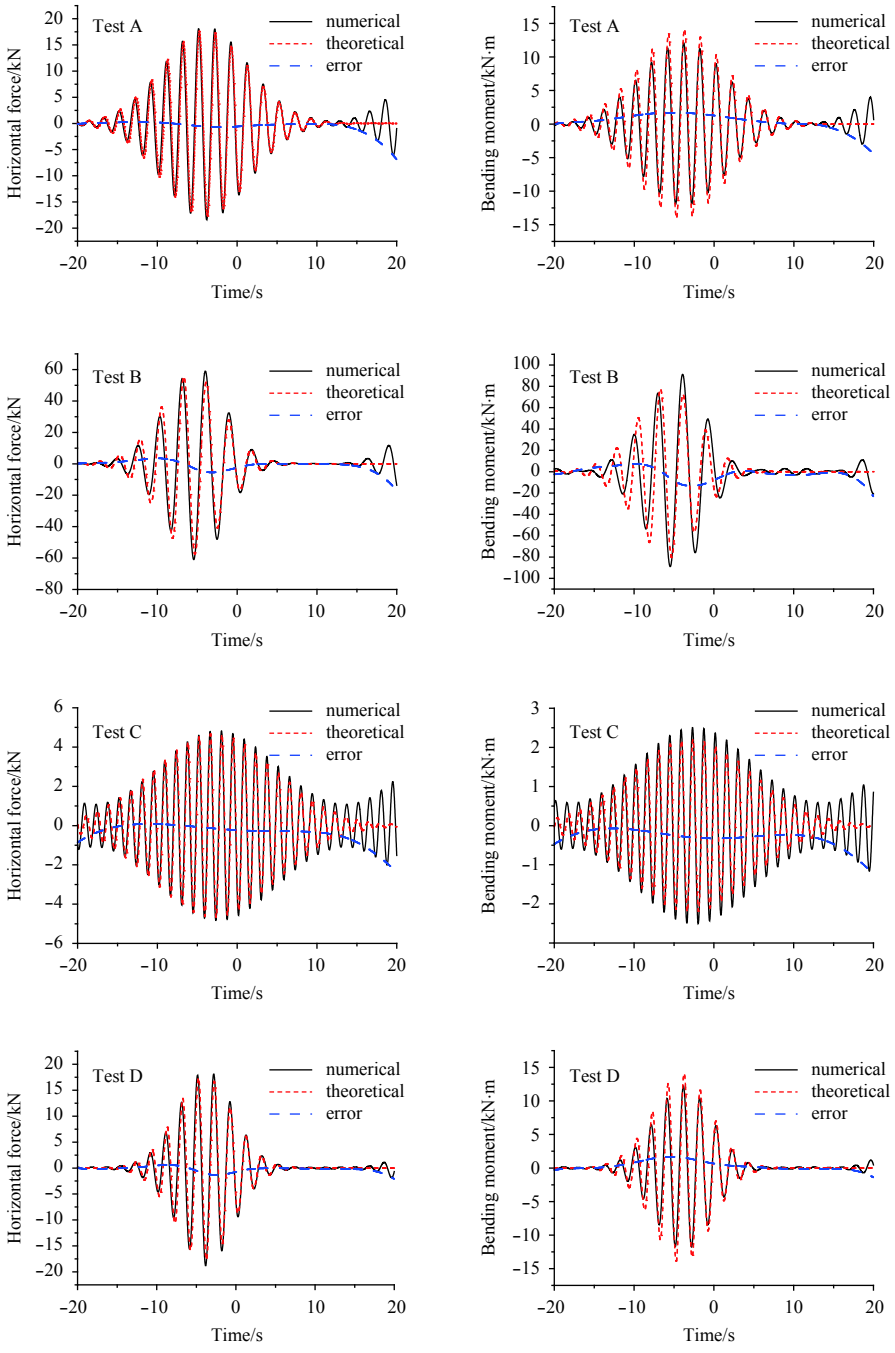

Fig. 13

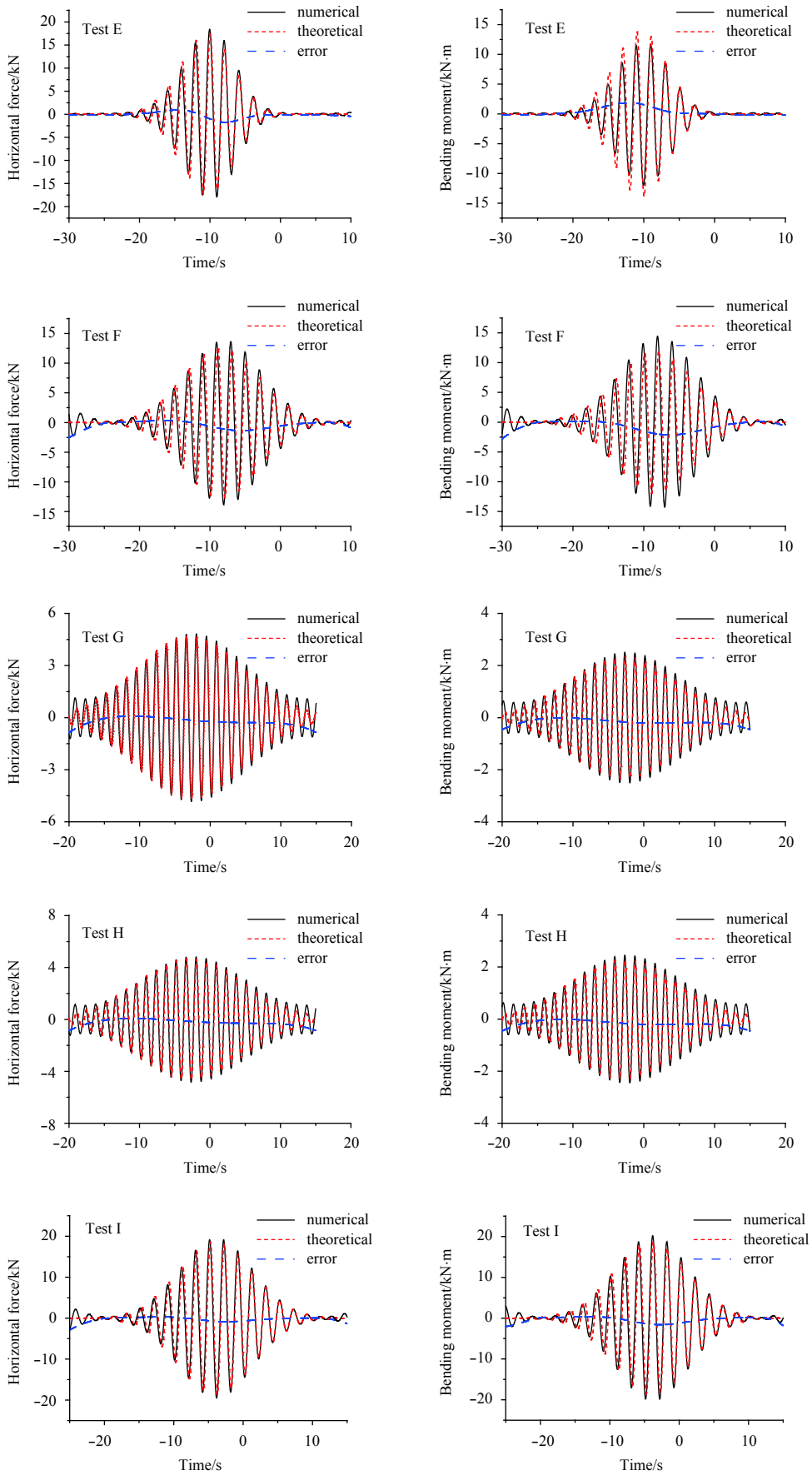
Test E
Horizontal force/kN
Bending moment/kN·m
Test F
Test G
Test H
Test I
numerical
theoretical
error
Time/s

Fig. 13

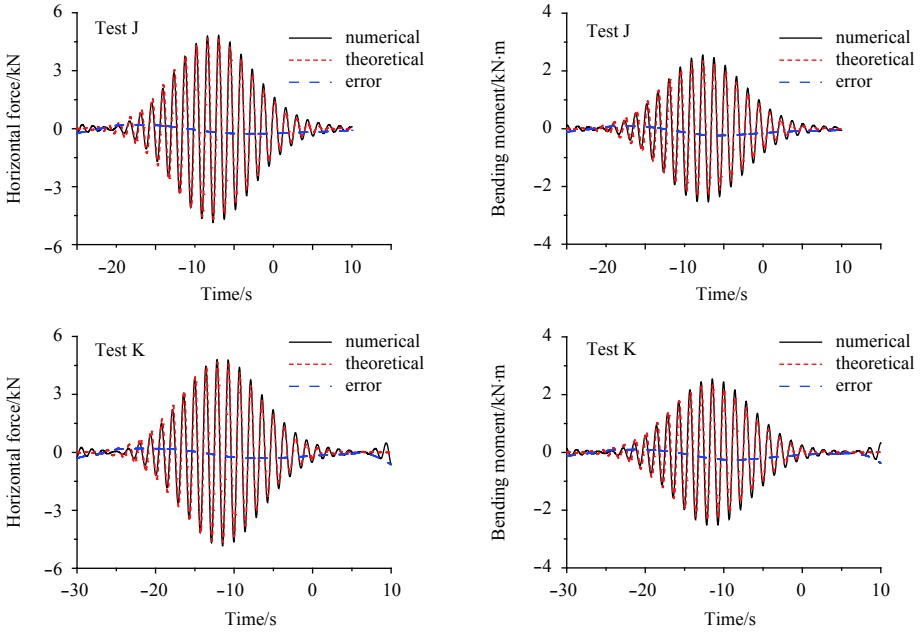

Fig. 13. Time series of horizontal force (left) and bending moment (right), predicted by theoretical formulas and WADAM.

5 Discussion

This section analyzes how the wave load changes with various parameters. First, by introducing non-dimensional variables $\bar{x}_0 = k_0 x_0$, $\bar{t} = \omega_0 t$, $\bar{h} = k_0 h$, $\bar{d} = k_0 d$, $\bar{R} = k_0 R$ and $\bar{\sigma} = k_0 \sigma$, the horizontal force and the bending moment can be nondimensionalized as follows:

$$\bar{F} = -\frac{Fk_0^2}{2\sqrt{2\pi}A_0\rho g}, \quad \bar{M} = -\frac{Mk_0^3}{2\sqrt{2\pi}A_0\rho g}. \tag{56}$$

Using Eq. (56), the wave load under the finite-depth and the deep water can be normalized as

$$\overline{F}_{\mathrm{fi}} = \overline{\sigma}\overline{R}\ \overline{W}_1\overline{X}, \tag{57}$$

$$\overline{M}_{\mathrm{fi}} = \overline{\sigma}\overline{R}\ \overline{W}_2\overline{X}, \tag{58}$$

$$\overline{F}_{\mathrm{de}} = \overline{\sigma}\overline{R}\ \overline{W}_3\overline{X}, \tag{59}$$

$$\overline{M}_{\mathrm{de}} = \overline{\sigma}\overline{R}\ \overline{W}_4\overline{X}, \tag{60}$$

where

$$\bar{W}_1 = \bar{W}_0 \frac{\sinh\bar{h} - \sinh\left(\bar{h}-\bar{d}\right)}{\cosh\bar{h}}, \tag{61}$$

$$\bar{W}_2 = \bar{W}_0 \left\{ \frac{\cosh\left(\bar{h}-\bar{d}\right) + \bar{d}\sinh\left(\bar{h}-\bar{d}\right)}{\cosh\bar{h}} - 1 + \frac{\bar{R}^2}{2}\frac{\sinh\left(\bar{h}-\bar{d}\right)}{\bar{h}\cosh\bar{h}} \right\}, \tag{62}$$

$$\bar{W}_3 = 1 - \mathrm{e}^{-\bar{d}}, \tag{63}$$

$$\bar{W}_4 = f_1\left(\mathrm{e}^{-\bar{d}} + \bar{d}\mathrm{e}^{-\bar{d}} - 1\right) + f_2\bar{R}^2\mathrm{e}^{-\bar{d}}, \tag{64}$$

$$\bar{W}_0 = \frac{1}{1 - \frac{4\sinh^2\left(\bar{h}-\bar{d}\right)}{2\bar{h}^2 + \bar{h}\sinh 2\bar{h}}\frac{\mathrm{H}_1\left(\bar{R}\right)}{\bar{R}\mathrm{H}'_1\left(\bar{R}\right)}}, \tag{65}$$

$$\bar{X} = \frac{1}{\sqrt{1/\bar{R}} + \mathrm{i}\sqrt{\bar{R}}}\frac{1}{\left(\bar{\sigma}^2 + \mathrm{i}\mu_1\bar{t}\right)^{1/2}} \times \exp\left[-\frac{\left(\bar{x}_0 + \mu_2\bar{t} + \bar{R}\right)^2}{4\left(\bar{\sigma}^2 + \mathrm{i}\mu_1\bar{t}\right)}\right]\mathrm{e}^{-\mathrm{i}\left(\bar{x}_0+\bar{t}+\bar{R}-\frac{3}{4}\pi\right)}, \tag{66}$$

$$\mu_1 = \frac{\omega''_0 k_0^2}{2\omega_0}, \quad \mu_2 = \frac{\omega'_0 k_0}{\omega_0}. \tag{67}$$

f_1 and f_2 of Eq. (64) are formulated in Eq. (32). Since the maximum force or moment is usually of interest for structure safety assessment, only the maximum crest of the load history is used in this section.

5.1 *The influence of* $\bar{x}_0$ *and* $\bar{\sigma}$

From Eqs (59)–(62), one can find that the focusing degree parameter $\bar{\sigma}$ and the focusing position $\bar{x}_0$ influence various sorts of wave load through the same term $\bar{\sigma}\bar{X}$, and that $\bar{x}_0 + \bar{R}$ can be treated as one variable in affecting the maximum wave load. Figure 14 investigates the influence of $\bar{\sigma}$ and $\bar{x}_0$ on term $\bar{\sigma}\bar{X}$. Although the focusing degree parameter $\bar{\sigma}$, when no cylinder exists within the flow field, does not affect the maximum crest height of the focusing wave, it can affect the wave load to some extent. In Fig. 14, the wave load increases with the growth of the energy focusing degree, although the rate of increasement seems to be unobvious if the focusing degree is already high enough. It is also found in Fig. 14 that the largest wave load occurs when $\bar{x}_0 + \bar{R}$ equals -1.5, and the smallest wave load happens when $\bar{x}_0 + \bar{R}$ equals 1.5. When $\bar{\sigma}$ is small, the relative positions of the focusing location and the cylinder can largely affect the wave load. To be

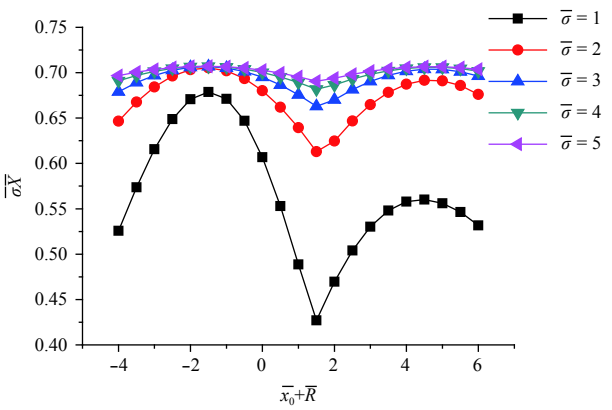

Fig. 14. The influence of $\bar{\sigma}$ and $\bar{x}_0$ on the maximum wave load, calculated with $\bar{R}=1$ and $k_0=1$.

specific, if the maximum wave crest occurs somewhere in front of the cylinder, i.e., the wave envelope reaches its highest wave height before it meets the cylinder, then large load can be induced. On the contrary, a small load is caused if the focusing position happens somewhere behind the cylinder. However, the influence of the focusing position becomes weak when the focusing degree parameter is big. For instance, $\bar{x}_0$ can hardly affect the wave load if $\bar{\sigma}$ equals 5 or larger.

5.2 *The influence of* $\bar{d}$

From Eqs (59)–(62), it is found that submerging depth $\bar{d}$ only affects terms $\bar{W}_1$ to $\bar{W}_4$. For the finite water depth, we let $\bar{h}=3$ and investigates the influence of $\bar{d}$, which varies from 1 to 3. Figure 15 shows the variation of the horizontal force (left) and the bending moment (right) under various $\bar{d}$. As is shown in Fig. 15a, the horizontal force rises with the growth of $\bar{d}$, which accords with common sense. However, by contrast, the bending moment experiences a decrescence at first and then begins to increase. At certain values of $\bar{d}$, the bending moment may decline to 0, due to the balance of the contributions from the load upon the side wall and upon the cylinder bottom. To be specific, when the submerging depth is small, the contribution from the cylinder bottom dominates the entire bending moment. However, with the increasement of the submerging depth, the influence of the side wall becomes significant, and meanwhile the contribution from the cylinder bottom is weaken since fluid particles away from the free surface almost keep still.

One may be interested in the relationship between $\bar{d}$ and $\bar{R}$ when the magnitude of bending moment reaches 0, which is revealed in Fig. 16. It can be seen that $\ln\bar{R}$ may be approximated by a linear function of $\bar{d}$, if $\bar{d}$ is not very close to $\bar{h}$. And it can be easily understood that $\bar{d}=\bar{h}$ is a singularity of the curves. It should be noted Eq. (60) begins to give incorrect results when $\bar{d}$ is less than $0.25\bar{h}$, which is decided empirically. For smaller $\bar{d}$ and larger $\bar{h}$, the deep-water approximation should be used.

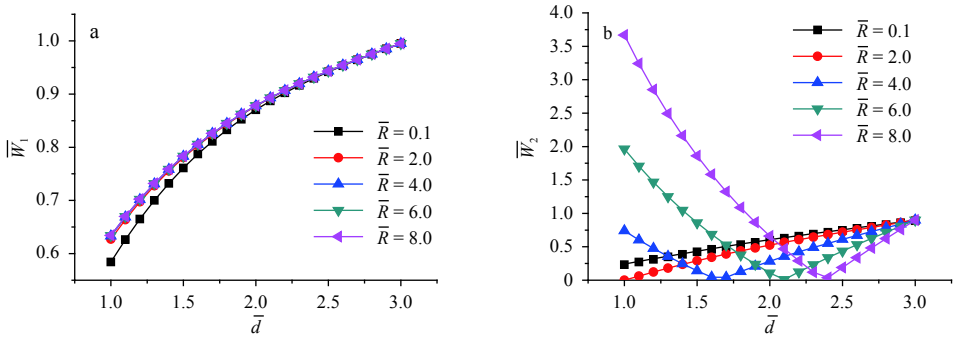

Fig. 15. The influence of $\bar{d}$ on the maximum wave load under the finite water depth, calculated with $\bar{h}=3$.

Similar to Fig. 15, Fig. 17 analyzes the influence of $\bar{d}$ on the horizontal force (left) and the bending moment (right) under the deep water, noted that $\bar{R}$ does not affect the value of $\bar{W}_3$. Also, similar to Fig. 15b, the bending moment under the deep water shows a piecewise linear pattern, yet the zero points of the bending moment under the deep water, which are illustrated in Fig. 18, differs from those under the finite-depth.

On the basis of the above discussions, one can find the focusing wave-induced loads exhibit many similarities with those induced by regular waves, which is due to the reason that a focusing wave is indeed dominated by a certain monochromatic regular wave. In general, the focusing wave induced loads is largely affected by the RAO of the carrier regular wave. Normally, RAO tends to be 0 when the wave frequency is either too small or too large. A small wave frequency indicates large wave lengths. Under the scale represented by the diameter of the cylinder, a large wave length leads to a mean free-surface elevation and a uniform flow field. Under such flow, both wave forces and wave moments are close to 0. On the contrary, the large wave frequency represents small waves, and a number of waves may exist within the length of the cylinder diameter. The loads induced by various waves are offset by each other, and hence a zero load is resulted. Usually a large wave force can be induced when the wave length is close to the cylinder diameter. However, this conclusion no longer applies for the wave moment, since the effects of both side walls and cylinder bottom need to be considered. Under certain

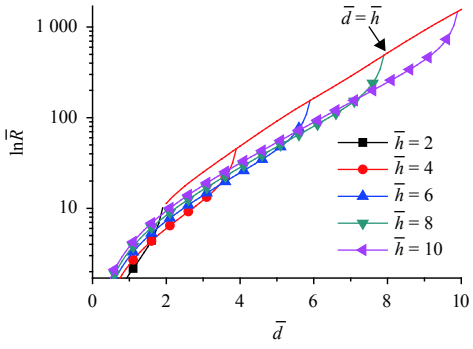

Fig. 16. The relationship between $\bar{d}$ and $\bar{R}$ when the bending moment reaches 0, under the finite water depth.

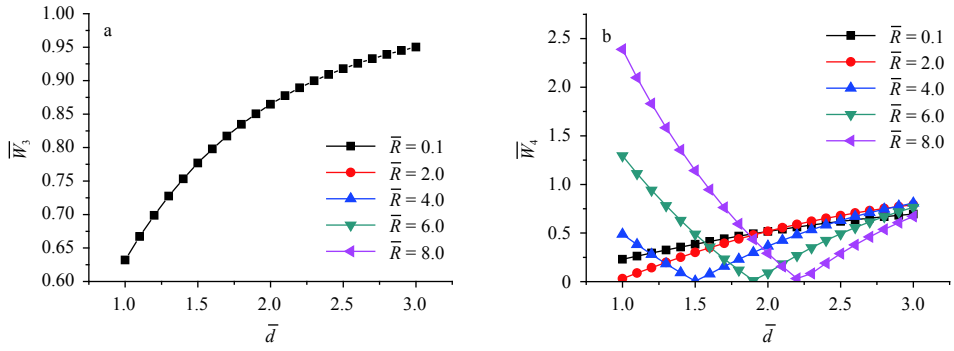

Fig. 17. The influence of $\bar{d}$ on the maximum wave load under the deep water.

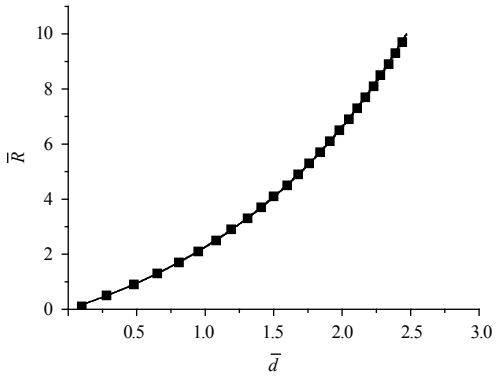

Fig. 18. The relationship between $\bar{d}$ and $\bar{R}$ when the bending moment reaches 0, under the deep water depth.

circumstances, the moment induced by the side wall may neutralize the one induced by the cylinder bottom, and a zero moment is produced. The above-mentioned phenomena can be found in both regular waves and focusing waves. However, the focusing waves are also characterized by focusing positions and focusing degrees, both of which can significantly affect the wave loads. The focusing degree is the first reason to be considered. To be specific, large focusing degrees correspond to large wave loads. Besides, the influence of the focusing positions can be neglected when the focusing degree is large. The focusing position only matters when the focusing degree is small enough. Usually, a large wave load happens when the focusing position is located somewhere in front of the fore edge of the cylinder, and a small load occurs when the focusing lies somewhere behind the aft edge of the cylinder.

6 Conclusions

In this paper, the wave-induced load is studied analytically, when a semi-submerged cylinder is placed in a focusing-wave flow field. The target focusing wave is modeled by the Gauss envelope and the expressions of the horizontal force and bending moment are given. For the convenience of engineering application, the derived formulas are sorted into two categories, i.e., the finite-depth solution and the deep-water solution, and are both simplified appropriately. The proposed formulas are verified by making comparison against the numerical results obtained using commercial potential-theory solver WADAM. In addition, the influence of parameters, such as the energy focusing degree, the wave focusing position and the submerging depth, is thoroughly investigated. During study, some meaningful conclusions are drawn as follows.

(1) The theoretical solution predicts results which agree well with the numerical simulation of WADAM, and this validates the formulas proposed in the paper.

(2) The progression solution converges so rapidly under the finite water depth that the leading order term is capable of predicting satisfying results. Yet the convergence rate becomes very slow under the deep water condition, and thereby requires modification or simplification.

(3) The wave load increases with the enhancement of the energy focusing degree. The wave load reaches its maximum value when the focusing position is located at the place where $\bar{x}_0 + \bar{R} = -1.5$ (or $x_0 = -R - 1.5/k_0$), and reaches its minimum value when the focusing position is at somewhere $\bar{x}_0 + \bar{R} = 1.5$ (or $x_0 = -R + 1.5/k_0$).

(4) The bending moment consists of the contributions from both the side wall and the cylinder bottom; however, these two kinds of moments can have opposite directions under certain condition. When the submerged depth is small, the contribution from the cylinder bottom dominates the total bending moment, yet the wave pressure upon the side wall becomes the main reason of the bending moment if the submerged depth is large. By carefully selecting the ratio of R to d, the bending moment may vanish.

References

Chabchoub A, Akhmediev N, Hoffmann N P. 2012a. Experimental study of spatiotemporally localized surface gravity water waves. Physical Review: E, 86: 016311

Chabchoub A, Hoffmann N P, Akhmediev N. 2011. Rogue wave observation in a water wave tank. Physical Review Letters, 106(20): 204502

Chabchoub A, Hoffmann N, Onorato M, et al. 2012b. Observation of a hierarchy of up to fifth-order rogue waves in a water tank. Physical Review: E, 86: 056601

Deng Yanfei, Yang Jianmin, Tian Xinliang, et al. 2016. Experimental investigation on rogue waves and their impacts on a vertical cylinder using the Peregrine breather model. Ships and Offshore Structures, 11(7): 757–765

Gao Ningbo, Yang Jianmin, Zhao Wenhua, et al. 2016. Numerical simulation of deterministic freak wave sequences and wave-structure interaction. Ships and Offshore Structures, 11(8): 802–817

He J S, Zhang H R, Wang L H, et al. 2013. Generating mechanism for higher-order rogue waves. Physical Review: E, 87: 052914

Hu Zhe, Tang Wenyong, Xue Hongxiang. 2014. Time-spatial model of freak waves based on the inversion of initial disturbance. Chinese Journal of Hydrodynamics (in Chinese), 29(3): 317–324

Hu Zhe, Tang Wenyong, Xue Hongxiang, et al. 2015. Numerical study of Rogue waves as nonlinear Schrödinger breather solutions

under finite water depth. Wave Motion, 52: 81–90

Hu Zhe, Xue Hongxiang, Tang Wenyong, et al. 2015a. Numerical study of nonlinear Peregrine breather under finite water depth. Ocean Engineering, 108: 70–80

Hu Zhe, Xue Hongxiang, Tang Wenyong, et al. 2015b. A combined wave-dam-breaking model for rogue wave overtopping. Ocean Engineering, 104: 77–88

Kharif C, Pelinovsky E. 2003. Physical mechanisms of the rogue wave phenomenon. European Journal of Mechanics -B/Fluids, 22(6): 603–634

Kit E, Shemer L, Pelinovsky E, et al. 2000. Nonlinear wave group evolution in shallow water. Journal of Waterway, Port, Coastal and Ocean Engineering, 126(5): 221–228

Qin Hao, Tang Wenyong, Xue Hongxiang, et al. 2017. Dynamic response of a horizontal plate dropping onto nonlinear freak waves using a fluid-structure interaction method. Journal of Fluids and Structures, 74: 291–305

Onorato M, Proment D, Clauss G, et al. 2013. Rogue waves: from nonlinear Schrödinger breather solutions to sea-keeping test. PLoS ONE, 8(2): e54629

Osborne A R, Onorato M, Serio M. 2000. The nonlinear dynamics of rogue waves and holes in deep-water gravity wave trains. Physics Letters: A, 275(5–6): 386–393

Slunyaev A, Clauss G F, Klein M, et al. 2013. Simulations and experiments of short intense envelope solitons of surface water waves. Physics of Fluids, 25: 067105

Soares C G, Fonseca N, Pascoal R, et al. 2006. Analysis of wave induced loads on a FPSO accounting for abnormal waves. Journal of Offshore Mechanics and Arctic Engineering, 128(3): 241–247

Sundar V, Koola P M, Schlenkhoff A U. 1999. Dynamic pressures on inclined cylinders due to freak waves. Ocean Engineering, 26(9): 841–863

Weerasekara G, Maruta A. 2017. Characterization of optical rogue wave based on solitons' eigenvalues of the integrable higher-order nonlinear Schrödinger equation. Optics Communications, 382: 639–645

Yu Fajun, Yan Zhenya. 2014. New rogue waves and dark-bright soliton solutions for a coupled nonlinear Schrödinger equation with variable coefficients. Applied Mathematics and Computation, 233: 351–358

Zakharov V E, Dyachenko A I, Prokofiev A O. 2006. Freak waves as nonlinear stage of Stokes wave modulation instability. European Journal of Mechanics-B/Fluids, 25(5): 677–692

Appendix A: Details on determination of $\alpha_{n,l}$ and $\gamma_{n,k}$

As has been mentioned, unknown $\alpha_{\mathrm{n,l}}$ and $\gamma_{\mathrm{n,j}}$ can be decided by using Eqs (3) and (4). Substituting Eqs (5), (9) and (10) into Eqs (3) and (4), the following equations can be obtained:

$$\sum_{n=0}^{\infty}\left\{\begin{array}{l}\alpha_{n,0}k\dfrac{\mathrm{H'}_n(kR)}{\mathrm{H}_n(kR)}\dfrac{\cosh[k(z+h)]}{\cosh kh}+\\ \dfrac{\mathrm{ig}\cosh k(z+h)}{\omega\cosh kh}k\beta_n\mathrm{J'}_n(kR)+\\ \sum\limits_{l=1}^{\infty}\alpha_{n,l}k_l\dfrac{\mathrm{K'}_n(k_lR)}{\mathrm{K}_n(k_lR)}\dfrac{\cos[k_l(z+h)]}{\cos k_lh}\end{array}\right\}\cos n\theta$$
$$=\left\{\begin{array}{ll}0 & -d<z<0\\ \sum\limits_{n=0}^{\infty}\left\{\begin{array}{l}\gamma_{n,0}\dfrac{n}{R}+\\ \sum\limits_{j=1}^{\infty}\gamma_{n,j}m_j\dfrac{\mathrm{I'}_n(m_jR)}{\mathrm{I}_n(m_jR)}\dfrac{\cos[m_j(z+h)]}{\cos m_jh}\end{array}\right\}\cos n\theta & -h<z<-d,\end{array}\right. \tag{A1}$$

$$\sum_{n=0}^{\infty}\left\{\begin{array}{l}\alpha_{n,0}\dfrac{\cosh[k(z+h)]}{\cosh kh}+\\ \dfrac{\mathrm{ig}\cosh k(z+h)}{\omega\cosh kh}\beta_n\mathrm{J}_n(kR)+\\ \sum\limits_{l=1}^{\infty}\alpha_{n,l}\dfrac{\cos[k_l(z+h)]}{\cos k_lh}\end{array}\right\}\cos n\theta=\sum_{n=0}^{\infty}\left\{\gamma_{n,0}+\sum_{j=1}^{\infty}\gamma_{n,j}\frac{\cos[m_j(z+h)]}{\cos m_jh}\right\}\cos n\theta\quad -h<z<-d-h<z<-d. \tag{A2}$$

Owing to the orthogonality of eigenfunctions, Eqs (A1) and (A2) yield a series of algebraic equations as follows

$$\alpha_{n,0}=-\frac{\mathrm{ig}\beta_n\mathrm{J'}_n(kR)\,\mathrm{H}_n(kR)}{\omega\mathrm{H'}_n(kR)}+\frac{n\sinh k(h-d)\cdot\mathrm{H}_n(kR)}{k^2R\cosh kh\cdot\mathrm{H'}_n(kR)\left\|Z_0\right\|^2}\gamma_{n,0}+$$
$$\sum_{j=1}^{\infty}\frac{m_j\mathrm{I'}_n(m_jR)\,\mathrm{H}_n(kR)\left\langle Z_0,\tilde{Z}_j\right\rangle}{k\mathrm{I}_n(m_jR)\,\mathrm{H'}_n(kR)\left\|Z_0\right\|^2}\gamma_{n,j}, \tag{A3}$$

$$\alpha_{n,l}=\frac{n\sin k_l(h-d)\,\mathrm{K}_n(k_lR)}{k_l^2R\cos k_lh\cdot\mathrm{K'}_n(k_lR)\left\|Z_l\right\|^2}\gamma_{n,0}+\sum_{j=1}^{\infty}\frac{m_j\mathrm{I'}_n(m_jR)\,\mathrm{K}_n(k_lR)\left\langle Z_l,\tilde{Z}_j\right\rangle}{k_l\mathrm{I}_n(m_jR)\,\mathrm{K'}_n(k_lR)\left\|Z_l\right\|^2}\gamma_{n,j}\quad l=1,\,2,\,3\ldots\ , \tag{A4}$$

$$\gamma_{n,0}=\frac{\mathrm{ig}\sinh k(h-d)\,\beta_n\mathrm{J}_n(kR)}{\omega kh\cosh kh}+\frac{\sinh k(h-d)}{kh\cosh kh}\alpha_{n,0}+\sum_{l=1}^{\infty}\frac{\sin k_l(h-d)}{k_lh\cos k_lh}\alpha_{n,l}\ , \tag{A5}$$

$$\gamma_{nj}=\frac{\mathrm{ig}\beta_n\mathrm{J}_n(kR)\left\langle Z_0,\tilde{Z}_j\right\rangle}{\omega\left\|\tilde{Z}_j\right\|^2}+\frac{\left\langle Z_0,\tilde{Z}_j\right\rangle}{\left\|\tilde{Z}_j\right\|^2}\alpha_{n,0}+\sum_{l=1}^{\infty}\frac{\left\langle Z_l,\tilde{Z}_j\right\rangle}{\left\|\tilde{Z}_j\right\|^2}\alpha_{n,l}\qquad j=1,2,3\ldots, \tag{A6}$$

where

$$\|Z_0\|^2=\int_{-h}^{0}\frac{\cosh^2[k(z+h)]}{\cosh^2 kh}\mathrm{d}z=\frac{1}{\cosh^2 kh}\left(\frac{h}{2}+\frac{\sinh 2kh}{4k}\right),$$

$$\|Z_l\|^2=\int_{-h}^{0}\frac{\cos^2[k_l(z+h)]}{\cos^2 k_l h}\mathrm{d}z=\frac{1}{\cos^2 k_l h}\left(\frac{h}{2}+\frac{\sin 2k_l h}{4k_l}\right),$$

$$\left\|\tilde{Z}_j\right\|^2=\int_{-h}^{-d}\frac{\cos^2[m_j(z+h)]}{\cos^2 m_j h}\mathrm{d}z=\frac{1}{\cos^2 m_j h}\left(\frac{h-d}{2}\right),$$

$$\left\langle Z_0,\tilde{Z}_j\right\rangle=\int_{-h}^{-d}\frac{\cosh[k(z+h)]}{\cosh kh}\times\frac{\cos[m_j(z+h)]}{\cos m_j h}\mathrm{d}z=\frac{1}{\cos kh\cos m_j h}\times\frac{(-1)^j k\sinh[k(h-d)]}{k^2+m_j^2},$$

$$\left\langle Z_l,\tilde{Z}_j\right\rangle=\int_{-h}^{-d}\frac{\cos[k_l(z+h)]\cos[m_j(z+h)]}{\cos k_l h\cos m_j h}\mathrm{d}z=\begin{cases}\dfrac{1}{Y}\dfrac{h-d}{2} & if\quad k_l=m_j\\ \dfrac{1}{Y}\left\{\begin{array}{l}\dfrac{\sin[(k_l+m_j)(h-d)]}{2(k_l+m_j)}+\\ \dfrac{\sin[(k_l-m_j)(h-d)]}{2(k_l-m_j)}\end{array}\right\} & \text{if}\quad k_l\neq m_j\end{cases},\tag{A7}$$

where $Y=\cos k_l h\cos m_j h$.

For realistic application, a finite number of expansion terms will be enough. Let $l=1,2,3,...,L$, $j=1,2,3,...,j$, $\boldsymbol{\alpha}_n=[\alpha_{n,0}\ \alpha_{n,1}\ \alpha_{n,2}\ ...\ \alpha_{n,L}]^{\mathrm{T}}$ and $\boldsymbol{\gamma}_n=[\gamma_{n,0}\ \gamma_{n,1}\ \gamma_{n,2}\ ...\ \gamma_{n,J}]^{\mathrm{T}}$, and Eqs (A3)–(A6) can be written in matrix as

$$\begin{pmatrix}\boldsymbol{E} & \boldsymbol{A}_n\\ \boldsymbol{B}_n & \boldsymbol{E}\end{pmatrix}\begin{pmatrix}\boldsymbol{\alpha}_n\\ \boldsymbol{\gamma}_n\end{pmatrix}=\begin{pmatrix}\boldsymbol{a}_n\\ \boldsymbol{b}_n\end{pmatrix},\tag{A8}$$

where

$$\left.\begin{aligned}
&(\boldsymbol{A}_n)_{1,1}=-\frac{n\sinh k(h-d)\times \mathrm{H}_n(kR)}{k^2R\cosh kh\times \mathrm{H}'_n(kR)\|Z_0\|^2},\ (\boldsymbol{A}_n)_{1,j+1}=-\frac{m_j\mathrm{I}'_n(m_jR)\mathrm{H}_n(kR)\left\langle Z_0,\tilde{Z}_j\right\rangle}{k\mathrm{I}_n(m_jR)\mathrm{H}'_n(kR)\|Z_0\|^2}\quad j=1,2,...,J,\\
&(\boldsymbol{A}_n)_{l+1,1}=-\frac{n\sin k_l(h-d)\mathrm{K}_n(k_lR)}{k_l^2R\cos k_l h\cdot \mathrm{K}'_n(k_lR)\|Z_l\|^2}\quad l=1,2,...,L,\\
&(\boldsymbol{A}_n)_{l+1,j+1}=-\frac{m_j\mathrm{I}'_n(m_jR)\mathrm{K}_n(k_lR)\left\langle Z_l,\tilde{Z}_j\right\rangle}{k_l\mathrm{I}_n(m_jR)\mathrm{K}'_n(k_lR)\|Z_l\|^2}\ \ l=1,2,...,L,\quad j=1,2,...,J,\\
&(\boldsymbol{B}_n)_{1,1}=-\frac{\sinh k(h-d)}{kh\cosh kh},\ (\boldsymbol{B}_n)_{1,l+1}=-\frac{\sin k_l(h-d)}{k_lh\cos k_lh}\quad l=1,2,...,L,\\
&(\boldsymbol{B}_n)_{j+1,1}=-\frac{\left\langle Z_0,\tilde{Z}_j\right\rangle}{\left\|\tilde{Z}_j\right\|^2}\quad j=1,2,...,J,\\
&(\boldsymbol{B}_n)_{j+1,l+1}=-\frac{\left\langle Z_l,\tilde{Z}_j\right\rangle}{\left\|\tilde{Z}_j\right\|^2}\\
&\qquad l=1,2,...,L,\quad j=1,2,...,J,\\
&(\boldsymbol{a}_n)_1=-\frac{\mathrm{ig}\beta_n\mathrm{J}'_n(kR)\mathrm{H}_n(kR)}{\omega\mathrm{H}'_n(kR)}\\
&(\boldsymbol{a}_n)_{l+1}=0\quad l=1,2,...,L\\
&(\boldsymbol{b}_n)_1=\frac{\mathrm{ig}\sinh k(h-d)\beta_n\mathrm{J}_n(kR)}{\omega kh\cosh kh}\\
&(\boldsymbol{b}_n)_{j+1}=\frac{\mathrm{ig}\beta_n\mathrm{J}_n(kR)\left\langle Z_0,\tilde{Z}_j\right\rangle}{\omega\left\|\tilde{Z}_j\right\|^2}\\
&\qquad j=1,2,...,J
\end{aligned}\right\}.\tag{A9}$$

Finally, $\alpha_{n,l}$ and $\gamma_{n,j}$ are calculated by solving Eq. (A8).

Appendix B: Deep-water approximation

Appendix A gives the exact way of determining $\alpha_{n,l}$ and $\gamma_{n,j}$ under various water depths. Here, simplification on Appendix A is made, under the condition that h $\to \infty$ and $d \to 0$.

Keeping only the leading order, the inner products listed in Eq. (A7) can be written as

$$\left.\begin{aligned} &\|Z_0\|^2 \to \frac{1}{2k} \\ &\|Z_l\|^2 \to \frac{1}{2\left(k_l h\right)^2} k^2 \cdot h^3 \\ &\left\|\tilde{Z}_j\right\|^2 \to \frac{h}{2} \\ &\left\langle Z_0, \tilde{Z}_j \right\rangle \to \frac{1}{k} \\ &\left\langle Z_l, \tilde{Z}_j \right\rangle \to -k \frac{1}{\left(k_l h\right)^2 - \left(m_j h\right)^2} \cdot h^2 \end{aligned}\right\}. \tag{B1}$$

Being decided by Eqs (8) and (11) respectively, k_l and m_j tends to 0 when $h \to \infty$. Therefore, the following limits exist:

$$\left.\begin{aligned} &\frac{m_j R \mathrm{I}'_1\left(m_j R\right)}{\mathrm{I}_1\left(m_j R\right)} \to 1 \\ &\frac{\mathrm{K}_1\left(k_l R\right)}{k_l R \mathrm{K}'_1\left(k_l R\right)} \to -1 \\ &\frac{m_j \mathrm{I}'_{\mathrm{n}}\left(m_j R\right) \mathrm{K}_n\left(k_l R\right)}{k_l \mathrm{I}_n\left(m_j R\right) \mathrm{K}'_{\mathrm{n}}\left(k_l R\right)} \to -1 \end{aligned}\right\}. \tag{B2}$$

Substituting Eqs (B1) and (B2) into Eqs (A3)–(A6), $\alpha_{n,l}$ and $\gamma_{n,j}$ are governed by equations as follows:

$$\alpha_{n,0} \to -\frac{\mathrm{i}g\beta_n \mathrm{J}'_n\left(kR\right) \mathrm{H}_n\left(kR\right)}{\omega \mathrm{H}'_n\left(kR\right)} + \sum_{j=0}^{\infty} \frac{2\mathrm{H}_n\left(kR\right)}{kR \mathrm{H}'_n\left(kR\right)} \gamma_{n,j} \ , \tag{B3}$$

$$\alpha_{n,l} \to \frac{2}{kh} \sum_{j=0}^{\infty} \frac{\left(k_l h\right)^2}{\left(k_l h\right)^2 - \left(m_j h\right)^2} \gamma_{n,j}, \tag{B4}$$

$$\gamma_{n,0} \to \frac{\mathrm{i}g\beta_n \mathrm{J}_n\left(kR\right)}{\omega kh} + \frac{1}{kh} \alpha_{n,0} - kh \sum_{l=1}^{\infty} \frac{1}{\left(k_l h\right)^2} \alpha_{n,l} \ , \tag{B5}$$

$$\gamma_{n,j} \to 2\frac{\mathrm{i}g\beta_n \mathrm{J}_n\left(kR\right)}{\omega kh} + 2\frac{1}{kh} \alpha_{n,0} - 2kh \sum_{l=1}^{\infty} \frac{1}{\left(k_l h\right)^2 - \left(m_j h\right)^2} \alpha_{n,l} \ . \tag{B6}$$